Unjamming overcomes kinetic and proliferation arrest in terminally differentiated cells and promotes collective motility of carcinoma

Andrea Palamidessi[1#], Chiara Malinverno[1,2,6 #], Emanuela Frittoli[1#], Salvatore Corallino[1], Elisa Barbieri[3], Sara Sigismund[2,3], Pier Paolo Di Fiore[2,3], Galina V. Beznoussenko[1], Emanuele Martini[1], Massimiliano Garre'[1], Dario Parazzoli[1], Ines Ferrara[4], Claudio Tripodo[4], Fabio Giavazzi[5,6], Roberto Cerbino[5,6], Giorgio Scita[1,3,6].

[1]IFOM, the FIRC Institute of Molecular Oncology, Via Adamello 16, 20139, Milan, Italy
[2]University of Milan, Department of Oncology and Hemato-Oncology, Via Festa del Perdono 7, 20122 Milan, Italy.
[3]Program of Molecular Medicine, European Institute of Oncology, Via Ripamonti 435, Milan, 20141, Italy
[4]Department of Health Sciences, Human Pathology Section, University of Palermo School of Medicine Via del Vespro 129, 90127, Palermo, Italy.
[5]University of Milan, Department of Medical Biotechnology and Translational Med., I-20090 Segrate, Italy

[#] These authors contributed equally to this work.

[6]These authors are all equally responsible for this work.

Correspondence to: Giorgio.Scita@ifom.eu or Chiara.Malinverno@ifom.eu or roberto.cerbino@unimi.it

Abstract

During wound repair, branching morphogenesis and carcinoma dissemination, cellular rearrangements are fostered by a solid-to-liquid transition known as unjamming. The biomolecular machinery behind unjamming, its physiological and clinical relevance remain, however, a mystery. Here, we combine biophysical and biochemical analysis to study unjamming in a variety of epithelial 2D and 3D collectives: monolayers, differentiated normal mammary cysts, spheroid models of breast ductal carcinoma in situ (DCIS), and *ex vivo* slices of orthotopically-implanted DCIS. In all cases, elevation of the small GTPase RAB5A sparks unjamming by promoting non-clathrin-dependent internalization of epidermal growth factor receptor that leads to hyper-activation of endosomally-confined ERK1/2 and phosphorylation of the actin nucleator WAVE2. Physically, activation of this pathway causes highly coordinated flocking of the cells, with striking rotational motion in 3D that eventually leads to matrix remodelling and collective invasiveness of otherwise jammed carcinoma. The identified endo-ERK1/2 pathway provides an effective switch for unjamming through flocking to promote epithelial tissues morphogenesis and carcinoma invasion and dissemination.

Introduction

Collective motility, a widely recognized mode of migration during embryogenesis, wound repair and cancer[1, 2], refers to the process of many cells migrating as a cohesive group with a high degree of coordination between neighbouring cells. A complex network of biochemical and physical interactions governs cellular and multicellular motility[2-5]. How cellular and supra-cellular biomechanics and biochemical wiring are integrated and impact onto each other remains, however, largely unexplored.

An emerging framework to interpret these interactions in unifying principles is the notion of cell jamming[6-8]. During tissue growth, cells are rather free to move around, as in a fluid. As density rises, the motion of each cell is constrained by the crowding due to its neighbours. At a critical density, motility ceases and collectives rigidify undergoing a liquid (unjammed)-to-solid (jammed) transition[6-8], herein referred to as UJT. This transition, which depends on a variety of biophysical parameters such as cell shape variance[9], intercellular adhesion, cortical tension and single cell motility, is thought to ensure proper development of barrier properties in epithelial tissues, but also to act as a tumour suppressive mechanism[6-8, 10]. The reverse jamming-to-unjamming transition (JUT) might, instead, represent a complementary gateway to epithelial cell migration, enabling tissues to escape the caging imposed by the crowded cellular landscape of mature epithelia[6, 10-12]. Indeed, whereas Epithelial-to-Mesenchymal Transition (EMT) has emerged as the overarching mechanism enabling the dissemination of single tumour cells[13, 14], invasion by epithelial malignancies (carcinomas) frequently involves the collective migration of cohesive cohorts (nests, sheets, or glandular/tubular structures) of cells into adjacent tissues rather than the scattering of individual carcinoma cells[15, 16]. A number of recent findings supports this hypothesis: i) breast carcinoma frequently disseminate by keeping their epithelial identity, i.e. tight cell-cell interactions and organization into cell cohorts or clusters[17, 18]; ii) circulating cancer cells efficiently seed distant metastasis by forming epithelial cell clusters that maintain cohesive cell-cell interactions, and by

69 doing so display increased metastatic seeding potential[19]; iii) histopathological studies suggest that
70 human invasive ductal breast carcinoma (DCIS) can invade collectively as strands or clusters that
71 retain E-Cadherin-based cellular junctions[20, 21]; iv) late-stage HER2-expressing murine mammary
72 cancers have been shown to undergo kinetic arrest and display reduced metastatic potential as a
73 consequence of increased density and cell packing[22, 23]. These findings further imply that mechanisms
74 capable of overcoming the jammed, kinetically silent state of advanced epithelial malignancies might
75 promote cancer dissemination without the need to invoke changes of cell identity or rewiring of
76 transcriptional programs. However, how cells control the JUT is unclear.

77 Membrane trafficking circuitries have emerged as pivotal in regulating the duration, intensity, and
78 spatial distribution of signals, thereby contributing to pathway specificity[24, 25], with a primary role on
79 cell migration plasticity and on the mechanics of cell-cell interactions[26-28]. Consistent with the above
80 notion, we recently found that endocytic circuitries controlled by RAB5A, a master regulator of early
81 endosomes necessary to promote a proteolytic, mesenchymal program of individual cancer cell
82 invasion[29, 30], have a dramatic impact on the mechanics and dynamics of multicellular, normal and
83 tumorigenic, cell assemblies[31]. Elevation of RAB5A levels is sufficient to re-awaken the motility of
84 otherwise jammed and kinetically arrested epithelial monolayers[31]. RAB5A does so by increasing
85 monolayers stiffness, cell-cell surface contact and junctional tension, while concomitantly
86 accelerating the turnover of junctional E-cadherin[31]. RAB5A further promotes millimetres-scale,
87 ballistic locomotion of multicellular streams by augmenting the extension of oriented and persistent
88 RAC1-driven, protrusions[31]. These effects combine to endow monolayers with a flocking fluid mode
89 of motion, which is explained in numerical simulations in terms of large scale coordinated migration
90 and local unjamming, driven by an increased capability of each individual cell to align its velocity to
91 the one of the surrounding group[31-33]. Molecularly, impairing endocytosis, macropinocytosis or
92 increasing fluid efflux abrogated RAB5A-induced collective motility, suggesting that perturbations
93 of trafficking processes impacting on different signalling and biomechanical pathways are necessary

94 for the JUT. However, the molecular nature of these endocytic-sensitive pathways remains to be
95 identified. Even less clear is whether JUT occurs in relevant physiological setting and whether is
96 hijacked by dense and jammed carcinoma to promote their collective dissemination.

97 Here, using kinematic and biochemical analysis of jammed monolayers dynamics, we showed that
98 enhanced epidermal growth factor receptor (EGFR) internalization through non-clathrin dependent
99 routes leads to endosomal ERK1/2 hyper-activation and phosphorylation of the branched actin
100 nucleator, WAVE2[34, 35]. This endo-ERK1/2 pathway, in turn, is critical to promote a transition to a
101 flocking-liquid mode of collective motility. Importantly, this pathway is also sufficient to overcome
102 kinetic and proliferation arrest of fully differentiated normal mammary cysts in 3D, and to initiate
103 bud morphogenesis. In DCIS models, instead, endocytic-mediated unjamming endows tumour
104 spheroids embedded into thick collagen matrix with a striking and coordinated circular angular
105 motion (CAM), that promotes matrix remodelling and collective local invasion, recapitulating what
106 is observed in DCIS foci orthotopically implanted into recipient mice. We propose that the EGF-
107 dependent activation of endosomal ERK1/2 as the first identified molecular route to the JUT via
108 flocking, sufficient to overcome the kinetic and proliferation arrest of terminal differentiated
109 epithelial cells, and to promote collective invasive programs of jammed breast carcinoma.

110 **Results**
111
112 **Endocytic reawakening of motility depends on EGFR activation and is caused by alterations of**
113 **EGFR trafficking**

114 RAB5A is deregulated in breast cancer (BC)[30, 36]. By focusing on early stages of BC progression, we
115 found that RAB5A expression was variably low in malignant cells of densely-packed and jammed
116 ductal carcinoma in situ (DCIS) foci and increased at foci of DCIS with invasion or in overt
117 infiltrating cancers (Fig.1A). Additionally, its elevated expression is detected in various malignant,
118 aggressive BC cell lines (Fig. 1B), and, more relevantly, correlates with worse relapse free probability
119 in various BC subtypes (Fig. S1). We employ doxycycline-inducible RAB5A-MCF10A-line to
120 induce the expression of the GTPase to levels that mimic those encountered in human DCIS (Fig.
121 1B), and study the molecular mechanisms of RAB5A impact on multicellular kinematics and
122 jamming transition[31]. Fully confluent, dense epithelial monolayers of normal mammary MCF10A
123 cells are locked into a jammed, solid state characterized by a full kinetic arrest (Ref.[31] and Movie
124 S1and S4). Doxycycline-mediated induction of RAB5A is sufficient to reawaken the motility by
125 promoting large cellular streams (Fig. 1C-D and Movie S1-4 and ref.[31]). Particle Image Velocimetry
126 (PIV) analysis was used to capture the kinematic of cell locomotion in jammed epithelia. As
127 previously reported[31], RAB5A expression enhanced robustly the root mean square velocity (v_{RMS}) of
128 the cells, and promoted millimetres-scale cell coordination as revealed by calculating the correlation
129 length, L_{corr}, as the width of the correlation function $C_{VV}(r) = \frac{\langle \boldsymbol{v}(\boldsymbol{x}_0+r)\cdot\boldsymbol{v}(\boldsymbol{x}_0)\rangle}{\langle|\boldsymbol{v}(\boldsymbol{x}_0)|^2\rangle}$ of the (vectorial) velocity
130 $v(x_0)$, whose typical width provides an estimate of the velocity correlation length[37]. We also
131 quantified cellular motion using the Mean Square Displacement (MSD) over a given time interval,
132 Δt, averaged over many cells in several optical fields (see Methods), which was used to extract an
133 estimate of the persistence length, L_{pers}[37]. The latter corresponds to the distance travelled by a cell at
134 constant velocity before the direction of its motion becomes uncorrelated with the initial one.
135 RAB5A-expression promoted persistent and ballistic collective motion over a distance larger than

136 700 μm, consistent with monolayers acquiring a flowing, liquid mode of motion. Removal of EGF,
137 required for proliferation and single cell motility of MCF10A[38], or addition of AG1478, an inhibitor
138 of EGFR kinase[39], arrested the flowing mode of motion induced by RAB5A (Fig. 1C-D and Movie
139 S1 and S2 and S4), reduced v_{RMS}, L_{corr}, and L_{pers} to values seen in control cells. These treatments
140 further impacted on the uniformity of the migration pattern captured by local alignment (a) of the
141 velocity vector with respect to the mean velocity, which varies between +1 and -1 when it is parallel
142 or antiparallel to the mean direction of migration, respectively (Fig. 1D). We further corroborated
143 these results using EGFP-H2B control and RAB5A-expressing cells to visualize directly nuclear cell
144 displacement within the epithelial collective (Movie S3). Finally, similar EGF–dependency of
145 collective motion was also observed in jammed keratinocyte monolayers, HaCat, (Ref.[31] and not
146 shown) and in oncogenically-transformed MCF10A variants, MCF10.DCIS.com (see below Fig. S5A
147 and Movie S16).

148 This finding is consistent with the possibility that alterations of endosomal biogenesis caused by
149 RAB5A[40] and leading to reawakening of collective motion[31] might specifically perturb EGFR cellular
150 distribution, trafficking or signalling. We set out to test these possibilities. Firstly, we showed that
151 the total protein, but not mRNA levels of EGFR were significantly reduced following induction of
152 RAB5A expression (Fig. 2A). The fraction of phosphorylated EGFR was, instead, unexpectedly
153 increased (Fig. 2A, Table), suggesting an impact of RAB5A on cellular distribution and trafficking
154 of this receptor. Consistently, immunofluorescent analysis revealed that RAB5A-expressing cells
155 display a marked reduction of cell surface EGFR, as detected in non-permeabilized cells,
156 accompanied by a sizable increase of intracellular EGFR, which accumulates in EEA1 positive
157 vesicle (Fig. 2B-C). Measurements of the absolute number of surface EGFR using ^{125}I-EGF binding
158 corroborated the immunofluorescence (IF) data (Fig. 2D). MCF10A are grown in the presence of
159 saturating dose of EGF (20 ng/ml), which binds and activates EGFR, promote its rapid internalization
160 and subsequent lysosomal degradation. Thus, RAB5A may perturb EGFR cellular distribution by

161 enhancing its internalization, trafficking and degradation. If this were the case removal of EGF or
162 inhibition of its kinase activity should restore EGFR surface and intracellular distribution to levels
163 seen in control cells. We verified this prediction by IF analysis (Fig. 2E-G), and by determining the
164 number of EGFR molecules on cell surface (Fig. 2H).

165 Intracellular accumulation of EGFR might be the results of elevated internalization or reduced
166 recycling. In the former case, although clathrin-mediated endocytosis (CME) represents the best-
167 characterized internalization route of EGFR into cells[41], it can also occur through non-clathrin
168 endocytosis (NCE), depending on growth conditions and cellular context[42-45]. At a low epidermal
169 growth factor (EGF) dose (1 ng/ml), EGFRs are primarily internalized by CME and recycled back to
170 the plasma membrane (PM)[44]. For large physiological EGF concentrations (20 to 100 ng/ml), NCE
171 is activated in parallel to CME. EGFRs entering via NCE (~40%) are predominantly trafficked to the
172 lysosome for degradation[44, 45]. To test whether RAB5A expression influences any of these entry
173 routes, we measured the rate of internalization of ^{125}I-EGF at low and high concentrations. RAB5A
174 expression significantly increased the endocytic rate constant (Ke) at high (30 ng/ml), but not at low
175 (1 ng/ml) EGF concentrations, suggesting a specific impact on NCE (Fig. 3A). Using a similar
176 approach, we also measured recycling rates of EGFR, which were not significantly altered by
177 elevation of RAB5A (Fig. 3B). Following doxycycline induction of RAB5A expression, we further
178 monitored the total levels of EGFR, which were slowly, but progressively decreased over time
179 consistently with the augmented NCE internalization into endocytic compartments (Fig. 3C).
180 Collectively, these findings indicate that RAB5A promotes EGFR NCE internalization routes, likely
181 leading to increased endosomal EGFR and, possibly, to the re-awakening of collective motion.

182

183 **Activation of endosomal ERK1/2 is a molecular route to unjamming via flocking**

184 EGFR signalling and trafficking are strictly interdependent[46]. For example, the detection of
185 phosphorylated receptors and signalling adaptors in endosomes indicated that signalling is initiated

186 at the plasma membrane but continues in endosomes[47-49]. Albeit recent work challenged this
187 concept[50, 51], quantitative high-resolution FRET microscopy demonstrated that phosphorylated EGFR
188 can be packaged at constant mean amounts in endosomes, which were proposed to act as signalling
189 quanta-like platforms[52]. As a consequence, altering the size and number of endosomes directly
190 affected the amplitude and duration of EGFR signalling.

191 Hence, we tested whether any of the canonical EGFR downstream pathways is altered following
192 RAB5A expression. We found that while phosphorylated AKT and p38 levels were not significantly
193 altered in confluent cells, phosphorylated ERK1/2 was elevated and long lived in RAB5A (Fig 4 A-
194 B), but not in RAB5B or C expressing cells (Fig. S2A-B). Notably, RAB5B and C were very
195 inefficient in reawakening collective motion in jammed monolayers (Fig. S2C and Movie S5). We
196 corroborated this finding by testing in situ, through IF, the levels of phosphorylated ERK1/2 in intact
197 monolayers formed by mixing control and EGFP-H2B-RAB5A-expressing cells (Fig. 4C). ERK1/2
198 has also been reported to be activated in a temporally distinct "two waves" fashion after wounding
199 that propagate in epithelial sheet controlling collective motion[53]. We found that RAB5A-MCF10A
200 cells, which display accelerated wound migration speed, display a robust increase in ERK1/2 wave
201 amplitude (Fig. S2D). Pharmacological inhibition of the ERK1/2 using PD0325901 that targets the
202 upstream MEK kinase[54], abrogated flocking mode of locomotion of RAB5A-monolayers by reducing
203 v_{RMS}, L_{corr} and L_{pers} to control levels (Fig. 4D and Movie S6). RAB5A-mediated elevation of ERK1/2
204 (Fig. 4E) was inhibited by treatment of MCF10A with AG1478 or Dynasore, a small molecule
205 impairing dynamin pinchase activity[55]. These treatments also impeded reawakening of collective
206 motion in jammed epithelia (Fig. 1, Movie S2, Movie S7 and ref[31]). Similar results were also obtained
207 by silencing the expression of Dynamin 2, the only dynamin isoform expressed in MCF10A (Fig.
208 S3A and Movie S8). The sum of these findings indicates that RAB5A elevation specifically enhances
209 endosomally-compartmentalized ERK1/2 signalling. To directly test this possibility, we generated
210 FRET EKAREV-ERK1/2 sensor[56], which was targeted to endosomes by appending to its C-terminus

211 the FYVE domain of SARA protein[57] (Fig. 4F). The FYVE-ERK1/2-EKAREV-FRET sensor was,
212 indeed, found on EEA1-positive endosomes (Fig. 4G), which were increased in size and dimension
213 following RAB5A expression[31]. Removal of EGF or treatment of cells with PD0325901, significantly
214 impaired FRET efficiency validating the biological relevance of the sensor (Fig. 4H). More
215 importantly, RAB5A-expressing cells displayed elevated endosomal ERK1/2 FRET efficiency as
216 compared to control monolayers (Fig. 4H). We further showed that global (or plasma membrane
217 associated) elevation of ERK1/2 phosphorylation brought about by the expression of a constitutively
218 activated MEK-DD stably expressed in MCF10A was insufficient to reawaken motility in jammed
219 monolayers (Fig. S3B-C and Movie S9), reinforcing the notion that ERK1/2 must be activated in
220 endosome to promote unjamming. Notably, inhibition of the late endosomal ERK1/2 scaffold, MP1or
221 p14[58, 59], had no impact on RAB5A mediated ERK1/2 hyper-activation, nor on collective motion (Fig.
222 S3D-F and Movie S10) suggesting that other, yet to be identified molecular determinants/scaffolds
223 mediate early endosome compartmentalization of ERK1/2 signalling.

224 What are the molecular substrates that endosomal ERK1/2 activates to promote collective motion?
225 RAB5A-expressing, unjammed monolayers move in a highly ballistic, directed fashion by extending
226 cryptic and oriented lamellipodia[60] underneath neighbouring cells[31]. The latter structures are
227 dependent on RAC1, which activates branched actin polymerization of the pentameric WAVE2
228 complex[61]. The key component of this complex, WAVE2, a nucleation promoting factor, must be
229 phosphorylated by ERK1/2 on multiple serine residues, among which S351 and S343, to be activated
230 and to control protrusion initiation and speed[62, 63]. Consistent with the latter finding, using
231 phosphospecific antibody, we found that RAB5A expression increased the phosphorylation of S351
232 and of S343 of WAVE2 (Fig. 5A) in an ERK1/2, EGFR and Dynamin-dependent manner (Fig. 5B).
233 Additionally, by monitoring the dynamics of cells mosaically-expressing EGFP-LifeAct, we found
234 that pharmacological inhibition of ERK1/2 impaired the formation of cryptic lamellipodia (Fig. 5C
235 and Movie S11). Thus, RAB5A promotes endosomal, EGFR-dependent ERK1/2 signalling leading

236 to hyper phosphorylation and activation of WAVE2, and the formation of persistent lamellipodia that
237 contribute to reawakening of collective motion.
238
239 **RAB5A-mediated unjamming overcomes kinetic and proliferation arrest in terminally-**
240 **differentiated mammary acini.**
241 To explore the biological consequence of RAB5A–induced endo-ERK1/2 axis in more relevant
242 physiological 3D processes, we exploited the well-established ability of MCF10A cells to recapitulate
243 mammary gland morphogenesis when grown in 3D on top of Matrigel plugs in Matrigel-containing
244 media[38]. Under these conditions, cells generate filled spheroid that within 14-to-21 days undergo a
245 full differentiation program, giving raise to apico-basally polarized (Fig. S4A), kinetically and
246 proliferation-arrested hollow cysts[38]. We employed mCherry-H2B-expressing control and RAB5A-
247 cells to monitor kinematics of differentiated cysts treated with doxycycline to induce transgene
248 expression (Fig. 6A). Cells in control differentiated acini display a limited motility and were, as
249 expected, locked in jammed, kinetically-arrested states. The expression of RAB5A reawakened
250 motility by triggering a striking circular angular rotational mode of motion with cells within the cysts
251 migrating in an apparent highly-coordinated fashion (Fig. 6B and Movie S12). We applied a custom
252 PIV analysis to evaluate the tangential velocity field associated with the cellular motion, from which
253 we extracted the relevant kinematic parameters, like the root mean square velocity v_{RMS} and the
254 rotational order parameter ψ (see Methods). The latter, which can vary in the range [0, 1], captures
255 the uniformity of collective motion (see also Methods): $\psi = 1$ corresponds to a rigidly rotating
256 sphere while, in the absence of coordinated motion, one expects $\psi \cong 0$. Control acini display barely
257 detectable v_{RMS}, while the order parameter Ψ was constantly below 0.2 (Fig. 6C and Movie S12-13).
258 In RAB5A-expressing cysts, we observed a marked elevation of ψ, which reached value close to 1
259 in correspondence of the largest values of v_{RMS}, reflecting the acquisition of collective angular
260 motion (CAM) (Fig. 6C and Movies S12-S13). We exploited this finding to assess whether RAB5A-

261 induced reawakening of motility in 3D cysts was dependent on the same key determinants controlling
262 2D locomotion using various inhibitors. Indeed, impairing EGFR activity, ERK1/2 phosphorylation
263 and dynamin-endocytosis effectively reduced v_{RMS} and the order parameter to control levels (Fig. 6C-
264 table and Movies S14). We further tested whether RAB5A promoted similar microscopic changes as
265 the ones seen in 2D unjammed monolayers[31]. Specifically, we analysed the morphology and
266 distribution of E-cadherin junction both by IF and phosphorylated ERK1/2. We observed that cells
267 in RAB5A-cysts display straight and compact junctions and elevated phosphoERK1/2 (Fig. S4B).
268 The junctional features likely account for the large scale, coordinated motility of RAB5A acini. We
269 also noticed that the induction of the expression of RAB5A in the initial phase of cystogenesis
270 reduced the number of acini, but the ones remaining were significantly larger in size (Fig. 6D and
271 Movie S15), and did not undergo proliferation arrest, like control cysts do. Indeed, whereas in control
272 acini we detected no Ki67-positive, proliferating cells after 14 days in overlaid cultures, a sizeable
273 fraction of RAB5A cysts kept on proliferating under conditions in which the number of apoptotic
274 cells was, instead, comparable to that of control acini (Fig. S4D). We investigated this phenotype
275 further by adding doxycycline to induce the expression of RAB5A at the end of the morphogenetic
276 process, when acini have ceased proliferation and motility to complete the differentiation program[38].
277 RAB5A expression reawakened not only cell motility (see above) but was also sufficient to overcome
278 proliferation arrest (Fig. 6F), in a strict ERK1/2-dependent manner (Fig. 6F).

279 The ERK1/2-dependent re-awakening of collective motion and proliferation of terminal
280 differentiated mammary glands has been associated with the initiation of a more complex program of
281 branched morphogenesis that begins with the formation of multicellular buds[64, 65]. The latter process
282 is thought to require in addition to specific growth factors, also the interaction of epithelial acini with
283 the microenvironment and ECM components[66-68]. Collagen Type I, for example, has been used to
284 increase mechanical tension and facilitate duct morphogenesis [69, 70]. Henceforth, we grew MCF10A
285 cells overlaid on mixed matrigel:collagen (5:1) gels[67, 71]. Under these conditions, cells form fully

286 differentiated acini undistinguishable from those grown on Matrigel only (Fig. 6G). Addition of
287 doxycycline to induce RAB5A expression, however, caused cysts to lose their spherical roundness,
288 and promoted the formation of multicellular buds (Fig. 6G). Thus, RAB5A-dependent reawakening
289 of cell motility occurs during 3D morphogenetic processes and enables to overcome proliferation
290 arrest in fully differentiated epithelial cell assemblies.
291

292 **Endocytic unjamming promotes collective invasion in BC DCIS spheroids and in ex vivo BC**
293 **foci**

294 The discovery that unjamming impacts on the collective motility and on the growth dynamics of
295 normal epithelial 3D ensembles prompted us to assess whether these processes can be exploited by
296 BC to enhance their collective motility and invasive dynamic behavior[72]. To this end, we generated
297 doxycycline-inducible MCF10.DCIS.com cells. These cells are isogenic to MCF10A, express
298 oncogenic T24-H-RAS, a relative rare mutation in human BC lesions, but were derived from
299 multiple-passage, murine orthotopic xenografts and shown to recapitulate in vivo and in vitro the
300 progression from DCIS to invasive carcinoma[73]. During the DCIS phase, they grow under intra-ductal
301 confinement where extreme cell packing and density exert mechanical stress, supress motility and
302 tumour progression. Consistently, MCF10.DCIS.com cells are locked in jammed kinetically arrested
303 state when plated at high confluency in 2D (Fig. S5A and ref.[31]). The expression of RAB5A promoted
304 the reawakening of collective motion (Fig. S5A and Movie 16 and ref.[31]). It also accelerated directed
305 motility of wounded monolayers, which instead of arresting after the opposing fronts collided, kept
306 on flowing as collective streams, reminiscent of "a wound that never heals[74]" (Fig. 7A ad Movie 17).
307 Biochemically, RAB5A expression decreased total EGFR levels, but robustly increased ERK1/2
308 without affecting AKT or p38 (which was slightly reduced) phosphorylation, as seen in
309 untransformed MCF10A cells (Fig. S5B).

310 In contrast with MCF10A, MCF10.DCIS.com cells form filled spheroids when grown in low
311 attachment, or on top or embedded in 3D ECM matrix, and can generate invasive 3D outgrowth
312 recapitulating DCIS-to-IDC conversion[75]. To test the impact of RAB5A-mediated unjamming on 3D
313 growth dynamic and collective invasion of MCF10.DCIS.com, we generated mCherry-H2B control
314 and RAB5A expressing cells, grew them as spheroids that were embedded in thick, native collagen
315 type I to recapitulate the desmoplastic reactive environments of DCIS. After doxycycline addition,
316 we monitored the spheroid kinematics. Whereas control cells display a slow, uncorrelated, disordered
317 motion (Fig. 7B and Movie S18), RAB5A-MCF-10.DCIS.com cells acquired a striking CAM,
318 displaying a remarkably large angular velocity Ω (of the order of ~12 rad/hr) and a strong persistence
319 in the orientation of the instantaneous axis of rotation captured by the decay time of the orientational
320 correlation function (the typical time interval over which the axis of rotation loses memory of its
321 initial orientation), which is of the order of minutes in control, but > 24hr in RAB5A-MCF-
322 10.DCIS.com spheroids (Fig. 7B). On top of this global rotational motion, a marked elevation of
323 fluid-like motility of the cells is also observed. The characteristic time scale associated with this
324 internal rearrangement dynamics is estimated by calculating the so-called overlap parameter Q (see
325 Methods for details). Briefly, Q is a function of time that decays from 1 to 0 according to the number
326 of nuclei that have been substantially displaced from their original position, when observed in a
327 reference frame co-moving with the whole spheroid (Fig. 7B). The decay of Q does not depend on
328 the rigid motion of the spheroid as a whole, but captures, instead, the "fluid-like" relative motion of
329 the cells.

330 Endocytic reawakening of liquid-like CAM in 3D RAB5A-MCF-10.DCIS.com spheroids was
331 dependent on EGFR activity, ERK1/2 phosphorylation, dynamin endocytosis and abrogated
332 following inhibition of ARP2/3-mediated branched polymerization (Fig 7C-table and Movies S19).
333 Furthermore, EM morphological analysis of control and RAB5A expressing monolayers, spheroids
334 and orthotopically-injected tumours revealed that RAB5A induces junctional straightening and

335 increases cell-cell surface contact areas (Fig. 7D). Thus, similar cellular/biochemical processes
336 driving 2D locomotion and 3D acini morphogenesis operate in controlling the dynamic behaviour of
337 oncogenic epithelial ensembles.

338 Next, we explored the pathological consequence of endocytic-mediated, unjamming of oncogenic
339 collectives. Using mixed EGFP-LifeAct and mCherry-H2B-expressing spheroids embedded into
340 collagen type I matrix, we monitored their behaviour over longer time scale. We invariably observed
341 that RAB5A promoted CAM, followed by the extension into the surrounding ECM of multicellular
342 protrusion in the form of invasive buds and strands, suggesting that unjamming and collective
343 invasion might be temporally coordinated and possibly coupled (Fig. 8A and Movie S20).

344 Collective invasion into native collagen type I, which, at the concentration used, form a very dense
345 network of intricate fibres, can only occur following its remodelling. Consistently, Second Harmonic
346 Generation (SHG) signals of two-photon illumination revealed that RAB5A-expressing spheroids
347 extensively remodelled the fibrillary collagen, generating gaps and channels for collective invasion
348 to occur (Fig. S5C and Fig. 8B). EGFR, ERK1/2, Dynasore, and ARP2/3 inhibitor of CAM prevented
349 also collagen remodelling and the formation of invasive buds, suggesting that acquisition of
350 unjamming in 3D promote collective invasion (Fig. 8B).

351 Finally, we tested the latter hypothesis in a closer to physio-pathological conditions using *ex vivo*
352 organotypic tumour slices from DCIS injected into the mammary fat pad of immunocompromised
353 mice. To this end, m-Cherry-H2B and EGFP-LifeAct-expressing-control and RAB5A-
354 MCF10.DCIS.com were xenotransplanted into NSG mice. After 4 weeks, tumour masses were
355 mechanically excised, and organotypic tissue slices were grown at the air-liquid interface (see
356 methods and ref.[76]). Under such conditions, bulk tumour tissues remain viable for up to 2 weeks and,
357 more importantly, their dynamic behaviour can be tracked over hours with high temporal resolution.
358 Control and RAB5A-DCIS organotypic cultures were exposed to doxycycline to induce transgene
359 expression and monitored by time lapse confocal microscopy. Whereas control tumours were largely

360 immobile (Fig. 8C and Movies S21), jammed and compacted, the expression of RAB5A induces
361 reawakening of cell dynamics. Cells became highly motile and appeared to stream in a way that
362 resembles currents in a river (Fig 8C and Movies S21). PIV analysis captured quantitatively the
363 transition to collective locomotory mode (Movie S22).

364 We concluded that endocytic unjamming of kinetically arrested dense DCIS tumours is sufficient
365 to instigate motility and to promote collective invasive behaviour.

366 **Discussion**

367 Here, we provide the first evidence for a novel molecular route to unjamming, which reinstates the
368 possibility of multicellular rearrangements in otherwise immobile mature epithelia and densely-
369 packed carcinoma. Biochemically, we showed that elevated NCE internalization of EGFR promotes
370 its accumulation into endosomal vesicles, which become proficient signalling platforms for the
371 prolonged and elevated activation of ERK1/2. Our data using an endosomal-FRET-ERK1/2 sensor
372 is, to our knowledge, the first direct demonstration of the latter contention. These findings are also
373 consistent with the notion that while ERK1/2 signalling initiates at the plasma membranes, it
374 continues into endosomes impacting not only on signal intensity and duration but also on specificity[46-
375 49, 77]. Accordingly, RAB5A-induced EGFR endosomal signalling promotes the hyper-
376 phosphorylation of WAVE2 that, by controlling branched actin polymerization, contributes to the
377 extension of oriented cryptic lamellipodia[60]. Physically, the latter protrusions exert increased traction
378 forces[31, 78], and enhance cell orientation, which is found to be the fundamental ingredient to obtain
379 liquid states with large Vičsek-like polar alignment, a signature of flocking in jammed epithelia[31-33].

380 It is likely that additional, not yet identified substrates are phosphorylated by endosomal ERK1/2.
381 Indeed, reawakening of motility in jammed epithelia requires perturbations of different cellular and
382 supra-cellular pathways and properties (including cell-cell adhesion, surface tension[79] and monolayer
383 rigidity[33] for optimal long-range force transmission[80], volume and density fluctuations[32, 81]), which
384 are all required to initiate a mode of locomotion that combines large scale correlation length with
385 increased local cell arrangement typical of fluidized RAB5A tissues. This notwithstanding, impairing
386 protrusion extension impedes the emergence of persistent flocking motion and abrogates the re-
387 awakening of motility, pointing to a major role of the protrusion extension mechanism in setting the
388 local directionality of the flocking motion.

389

390 Our results also represent a step forward in addressing the physio-pathological relevance of tissue
391 *unjamming*. In 3D morphogenetic assays of mammary gland morphogenesis, we showed that endo-
392 ERK1/2-mediated unjamming not only promotes the acquisition of coordinated angular rotational
393 mode of motion, but that it is sufficient to overcome differentiation-induced proliferation arrest.
394 These latter two features combine with input arising from the presence of collagen type I in the
395 substrate, which likely provides increased mechanical tension[69-71, 82], to facilitate multicellular bud
396 formation, a process marking the beginning of branching morphogenesis[68]. Indeed, local elevation of
397 ERK1/2, promoting both re-entry into proliferation and collective motion, has been shown to mediate
398 murine mammary gland branching morphogenesis[64, 65], remarkably similar to what we observe in our
399 in vitro 3D assays. Thus, we argue that the endocytic-dependent jamming transition molecularly
400 described here might be a valuable framework to account for the initiation of complex morphogenetic
401 processes.

402 Finally, we showed that Endo-ERK1/2-unjamming might also be sufficient to overcome the
403 rigid, kinetically-silent state of packed epithelial carcinoma spheroids that grow confined and encased
404 by a thick collagen type I matrix. Endocytic unjamming, here, leads to the acquisition of flocking
405 fluid modes of motion, in which highly coordinated and collective rotational migration and local
406 unjamming coexist, providing the first evidence that this transition occurs not only in 2D monolayers,
407 but also in complex 3D environments. Re-awakening of collective motion, under these conditions, is
408 accompanied by a dramatic remodelling of the ECM and by the extension of collective invasive buds
409 and strands. This process recapitulates some aspects of the transition from DCIS, which grow under
410 intra-ductal confinement where extreme cell packing and density exert mechanical stress, supress
411 motility and tumour progression, to invasive carcinoma, which disperse locally also through
412 collective invasion[83]. We showed that RAB5A is elevated in various human breast cancer subtypes
413 and its elevated expression correlates with reduced relapse free probability, supporting the notion that
414 jamming transition might, indeed, be an additional mechanism to promote local collective invasion

415 of densely packed breast carcinoma. In this setting, RAB5A induction could be an alternate route to

416 EGFR addiction in invasive breast carcinomas, independently of HER2 status.

417

418 **Methods**

419 Methods and any associated accession codes and references are included after the references.

420

421 **Acknowledgments**

422 This work has been supported by: the Associazione Italiana per la Ricerca sul Cancro (AIRC) to GS
423 (IG#18621), PPDF (IG#18988 and MCO 10.000); the Italian Ministry of University and Scientific
424 Research (MIUR) to PPDF; the Italian Ministry of Health (RF-2013-02358446) to GS. Regione
425 Lombardia and CARIPLO foundation (Project 2016-0998) to RC; Worldwide Cancer Research
426 (WCR#16-1245) to SS. CM and FG are partially supported by fellowships from the University of
427 Milan, EB from the FIRC-AIRC.

428

429

430 **Author contributions**

431 AP, CM, EF design and perform all the experiments and edited the manuscript, SC aid in generating
432 cell lines and in the analysis of IF and kinematic studies, SB, SS and PPFD conceived internalization
433 assays and interpreted trafficking results, GVB perform EM studies, EM, MG, and DP aided in all
434 the imaging acquisition, FRET and PIV analysis, CT aided in analysis of RAB5A expression in BC,
435 FG and RC analyzed all the kinematic data and developed pipeline for the analysis of 3D motility,
436 edited the manuscript and conceived part of the study together with CM, GS conceived the whole
437 study, wrote the manuscript and supervised the whole work.

438

439 **Competing financial interests**

440 The authors declare no competing financial interests.

441

442 **Data Availability Statement**

Codes used for the analysis are all indicated in the methods section. The authors declare that all data supporting the findings of this study are available within the paper and its supplementary information files and there no restriction on data availability.

Figure 1

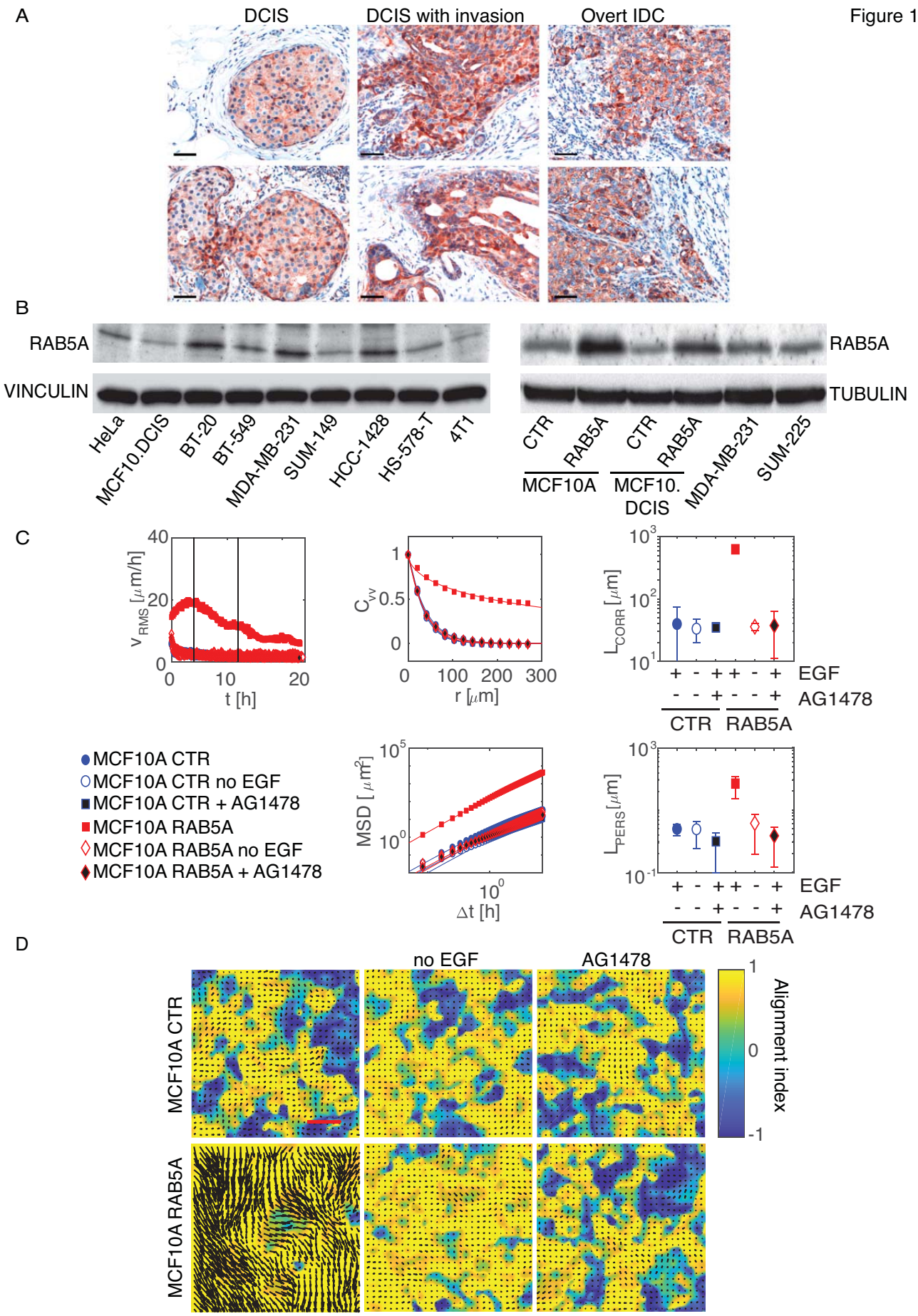
A
DCIS
DCIS with invasion
Overt IDC
B
RAB5A
VINCULIN
HeLa
MCF10.DCIS
BT-20
BT-549
MDA-MB-231
SUM-149
HCC-1428
HS-578-T
4T1
RAB5A
TUBULIN
CTR
RAB5A
CTR
RAB5A
MDA-MB-231
SUM-225
MCF10A
MCF10. DCIS
C
v_{RMS} [μm/h]
t [h]
C_{vv}
r [μm]
L_{CORR} [μm]
EGF
AG1478
CTR
RAB5A
MCF10A CTR
MCF10A CTR no EGF
MCF10A CTR + AG1478
MCF10A RAB5A
MCF10A RAB5A no EGF
MCF10A RAB5A + AG1478
MSD [μm^2]
Δt [h]
L_{PERS} [μm]
D
no EGF
AG1478
MCF10A CTR
MCF10A RAB5A
Alignment index

447

448 **Figure 1. Endocytic reawakening of motility is strictly dependent on EGFR activation**

449 **A.** Representative immunohistochemical staining of RAB5A on human ductal breast carcinoma in
450 situ (DCIS) foci, DCIS with invasive components, and overtly infiltrative breast cancer foci showing
451 the heterogeneous expression of RAB5A in DCIS foci and its increase in invasive areas. Scale bar,
452 100 μm. Please note the heterogenous and elevated expression of RAB5A in human IDC vs DCIS.

453 **B**. Doxycycline-treatment of MCF10A and MCF.DCIS.com engineered to express RAB5A in an
454 inducible fashion increases the level of the protein, mimicking those found a variety of BC lines
455 shown in the lower panels. Immunoblotting of total cell lysates with the indicated abs. Tubulin and
456 Vinculin were used as loading control.

457 **C**. PIV analysis of motion of doxycycline-treated control and RAB5A-MCF10A cells seeded at a
458 jamming density and monitored by time-lapse microscopy in the presence or the absence of EGF
459 (Movie S1 and 3) or after treatment with the EGFR inhibitor AG1478 (Movie S2). Vertical lines
460 indicate the time interval used for the analysis of the following motility parameters: $v_{RMS} = \sqrt{\langle |\boldsymbol{v}|^2 \rangle}$:
461 root mean square velocity (representative of > 5 independent experiments); C_{VV}: velocity correlation
462 functions as function of the distance r. The correlation function is evaluated in the time window
463 comprised between 4 and 12 h during which a peak in v_{RMS} is observed. In all cases, C_{VV} is well
464 fitted to a stretched exponential decay, with stretching exponent γ decreasing from 0.91±0.06
465 (control) to 0.62±0.04 (RAB5A). L_{corr}: correlation lengths whose width provide an estimate of the
466 size of group of cells moving in coordinated fashion, which in RAB5A-expressing cells is close to
467 0.78±0.3 mm, (corresponding to more than 50 cell diameter), whereas in control or after EGF-
468 deprivation or treatment with AG1478 is around 44±6 μm (1-to-2 cell diameter). MSD: mean square
469 displacements obtained by numerical integration of the velocity maps over a given time interval, Δt.
470 In all cases, for short times MSD displays a quadratic scaling $MSD \cong (u_0 \Delta t)^2$, which is indicative
471 of a directed ballistic motion, although with dramatically different characteristic velocities (u_0=36
472 μm/h for RAB5A, u_0< 7 μm/h for the control or w/ o EGF or in the presence of AG1578). At later

473 times, a transition to a diffusive-like regime characterized by a scaling exponent close to 1 is
474 observed. By fitting the MSD curves with a model function (continuous lines-see methods), we
475 extracted an estimate of a persistence lengths, $L_{pers,}$ which in RAB5A is around 450±50, while in all
476 other conditions is less than 65±3.1.
477 Data were obtained by analysis of at least 5 movies/experimental conditions out of at least 4
478 independent experiments.
479 **D**. Snapshots of the velocity field obtained from PIV analysis of doxycycline-treated control (Ctrl)
480 and RAB5A-MCF-10A cells seeded at jamming density in the presence or the absence of EGF or
481 treated with the EGFR inhibitor, AG1478, and monitored by time-lapse microscopy (Movie S4). The
482 colour-map reflects the alignment with respect to the mean instantaneous velocity, quantified by the
483 parameter $a(x) = (\boldsymbol{v}(x) \cdot \boldsymbol{v}_0)/(|\boldsymbol{v}(x)||\boldsymbol{v}_0|)$. $a = 1(-1)$, the local velocity is parallel (antiparallel) to
484 the mean direction of migration (not shown). Scale Bar, 100 μm.

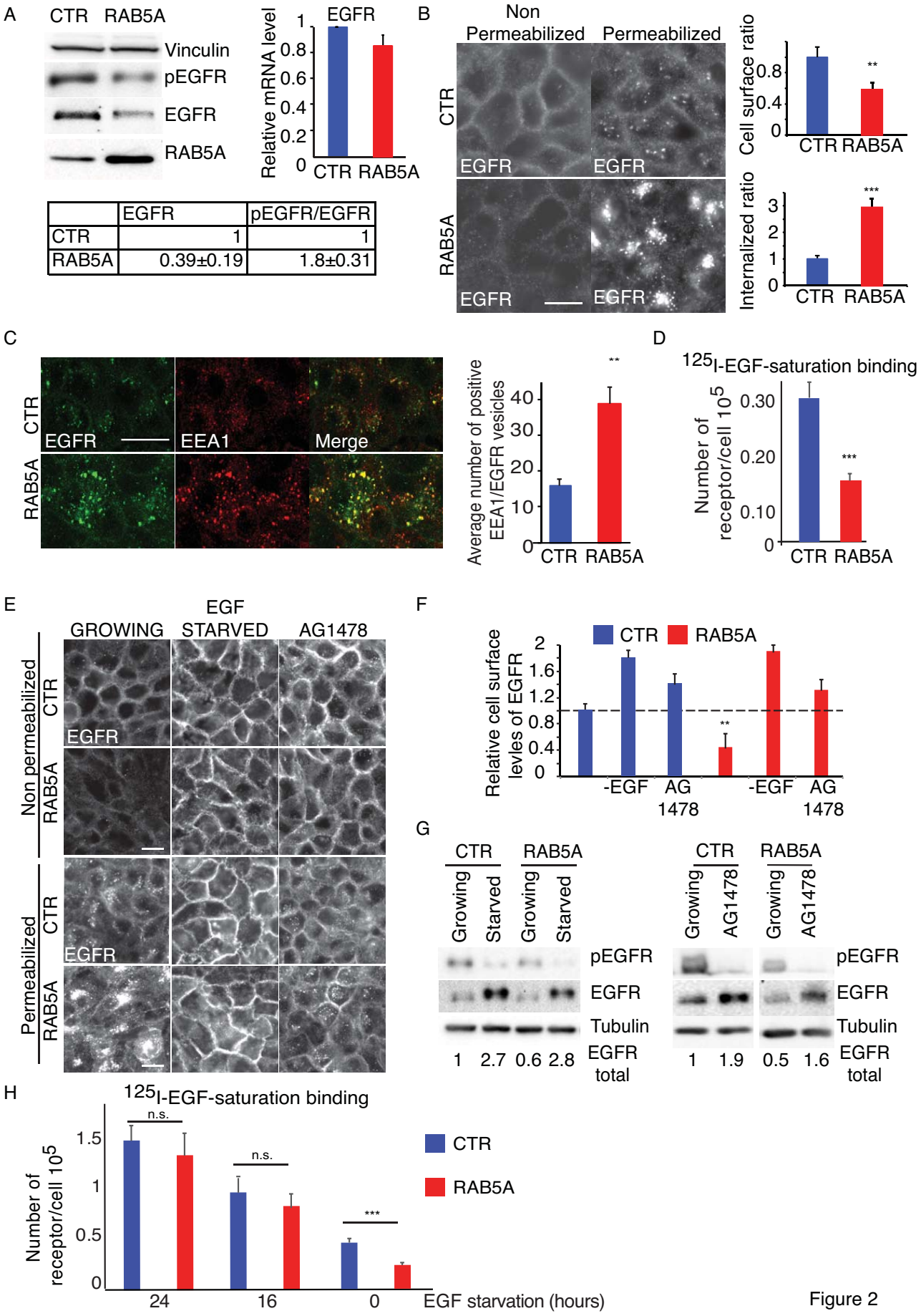

	EGFR	pEGFR/EGFR
CTR	1	1
RAB5A	0.39±0.19	1.8±0.31

Figure 2

486 **Figure 2. RAB5A alters EGFR cellular distribution, trafficking and stability.**

487 **A.** Total cellular proteins (left) and EGFR mRNA levels (right) of control (CTR) and RAB5A-
488 MCF10A seeded at jamming density and detected by immunoblotting or qRT-PCR, respectively. At
489 the bottom, quantification of total EGFR and of the ratio of phosphorylated/total EGFR from the
490 immunoblotting is shown. Data are the relative ratio (mean±SD, n=5 independent experiments) with
491 respect to control, obtained after normalizing each intensity values to Vinculin. The levels of EGFR
492 mRNA are expressed relative to control (mean±SD, n=5 independent experiments) after normalizing
493 to GAPDH.

494 **B.** Control and RAB5A-MCF10A cells seeded at a jamming density were fixed and either
495 permeabilized or non-permeabilized with 0.1% Triton X100 before staining with anti-EGFR ab. Data
496 are the relative ratio (mean ± SD) with respect to control of total cell surface or internalized EGFR
497 signals (n = 100 cells out of at least 3 independent experiments) normalized to cell number. Scale
498 Bar, 20 μm.**p< 0.01, ***p<0.005. *P* values were calculated using each-pair Student's t-test.

499 **C.** Representative images of control and RAB5A-MCF10A cells seeded at a jamming density, fixed
500 and stained with the indicated abs. Data are the mean±SD of positive EEA1and EGFR vesicles/cells
501 (n>150 out of 3 independent experiments). ** p< 0.01, Student's t-test. Scale Bar, 20 μm

502 **D.** Number of EGFR/cell of control and RAB5-MCF10A seeded at jamming density measured by
503 ^{125}I-EGF saturation binding after subtracting unspecific background counts (see methods for details).
504 Data are the mean±SD of triplicate measurements of a representative experiment. *** p<0.005. *P*
505 values were calculated using each-pair Student's *t* test.

506 **E-G**. Representative images (**E**) of control and RAB5A-MCF10A cells seeded at a jamming density,
507 which were either deprived of EGF for 24 h or treated with AG1478 before fixation and staining as
508 described in B. Scale Bar, 20 μm. Data (**F**) are the relative ratio (mean ± SD) with respect to control
509 of total cell surface EGFR (n>120 cells in 2 independent experiments) normalized to cell number. **
510 p<0.05, each-pair Student's t-test versus control. Immunoblots (**G**) showing the efficacy of EGF

511 deprivation and EGFR inhibition on total and phosphorylated EGFR levels using the indicated abs.
512 Each band of total EGFR was quantified and its mean intensity value is shown. The experiment is
513 representative of at least 5 independent ones with similar outcome.
514 **H.** Number of EGFR/cell of control and RAB5-MCF10A seeded at jamming density measured by
515 ^{125}I-EGF saturation binding after various time of EGF starvation as described in D. Data are the
516 mean±SD of triplicate measurements of representatives experiments. * $p<0.05$. *P* values were
517 calculated using each-pair Student's t-test.
518

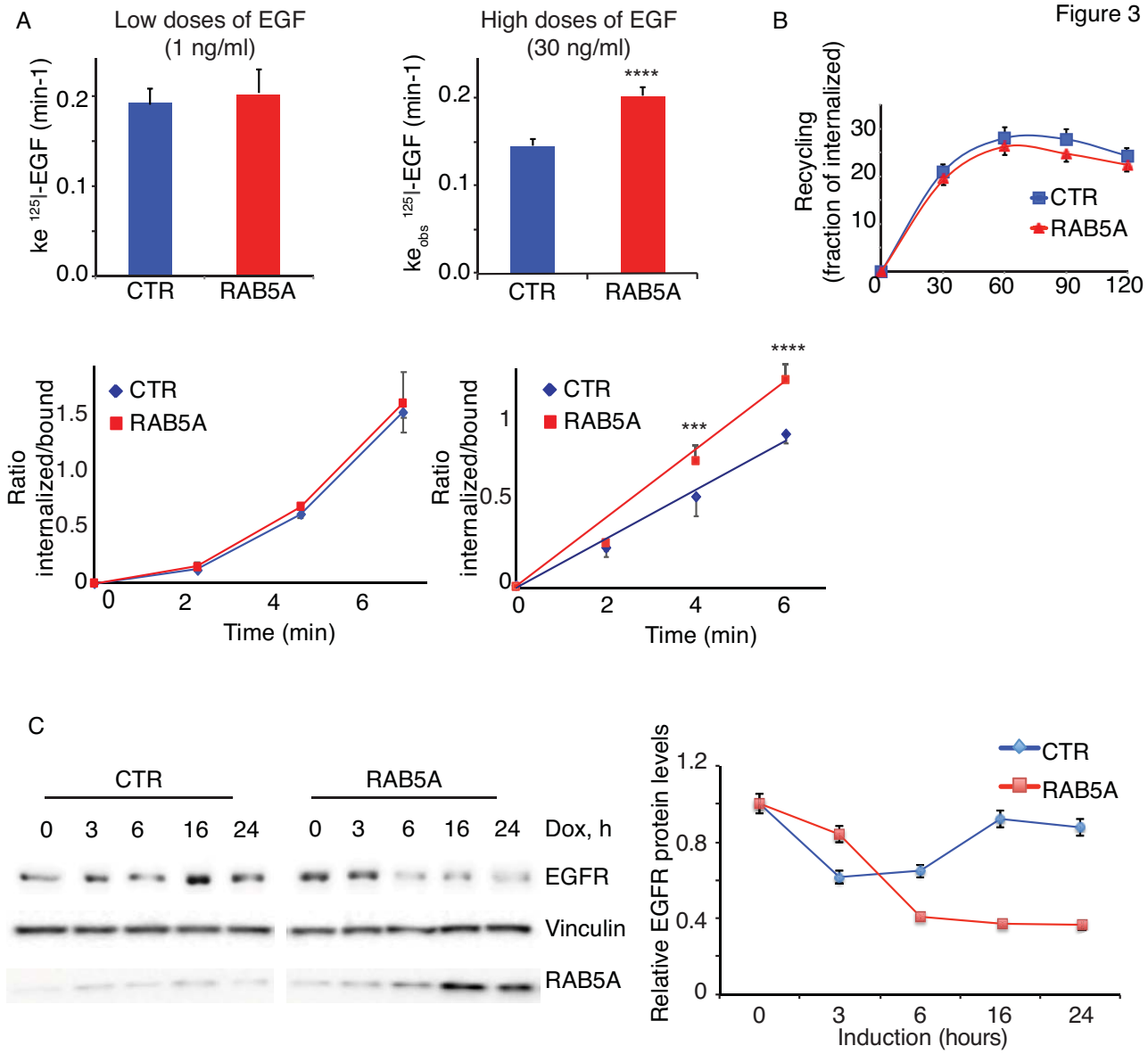

519

520 **Figure 3. RAB5A enhances internalization of EGFR at high doses of ligand.**

521 **A.** EGFR internalization kinetics in control and RAB5A-MCF10A cells seeded at jamming density
522 was measured using ^{125}I-EGF at low (1 ng/ml) or high (30 ng/ml) concentrations. Results are
523 expressed as the effective or apparent internalization rate constants at low and high EGF doses,
524 respectively (Ke, upper panel). A representative kinetic of the ratio of ^{125}I-EGF internalized/bound is
525 shown at different time points and is expressed as the mean±SD (n=3 out of 5 independent
526 experiments). ****p <0.0005. *P* values were calculated using each-pair Student's t-test.

527 **B**. Control or RAB5A-MCF10A cells seeded at jamming density were incubated with ^{125}I-EGF (30
528 ng/ml) for 15 min at 37 ˚C. Recycling of ^{125}I-EGF at the indicated time points was estimated as
529 described in Methods. Data are the mean ± SD (n = 3 replicates in a representative experiment).
530 **C**. A representative kinetic of total EGFR levels as function of time after treatment with doxycycline
531 in control or RAB5A-MCF10A cells. At the indicated time, total cellular lysates were immunoblotted
532 with the indicated abs. The EGFR levels relative to control and normalized to Vinculin, used as loaded
533 control are shown. Data are the mean±SD (n=5 independent experiments). Representative blots are
534 shown.
535

Figure 4

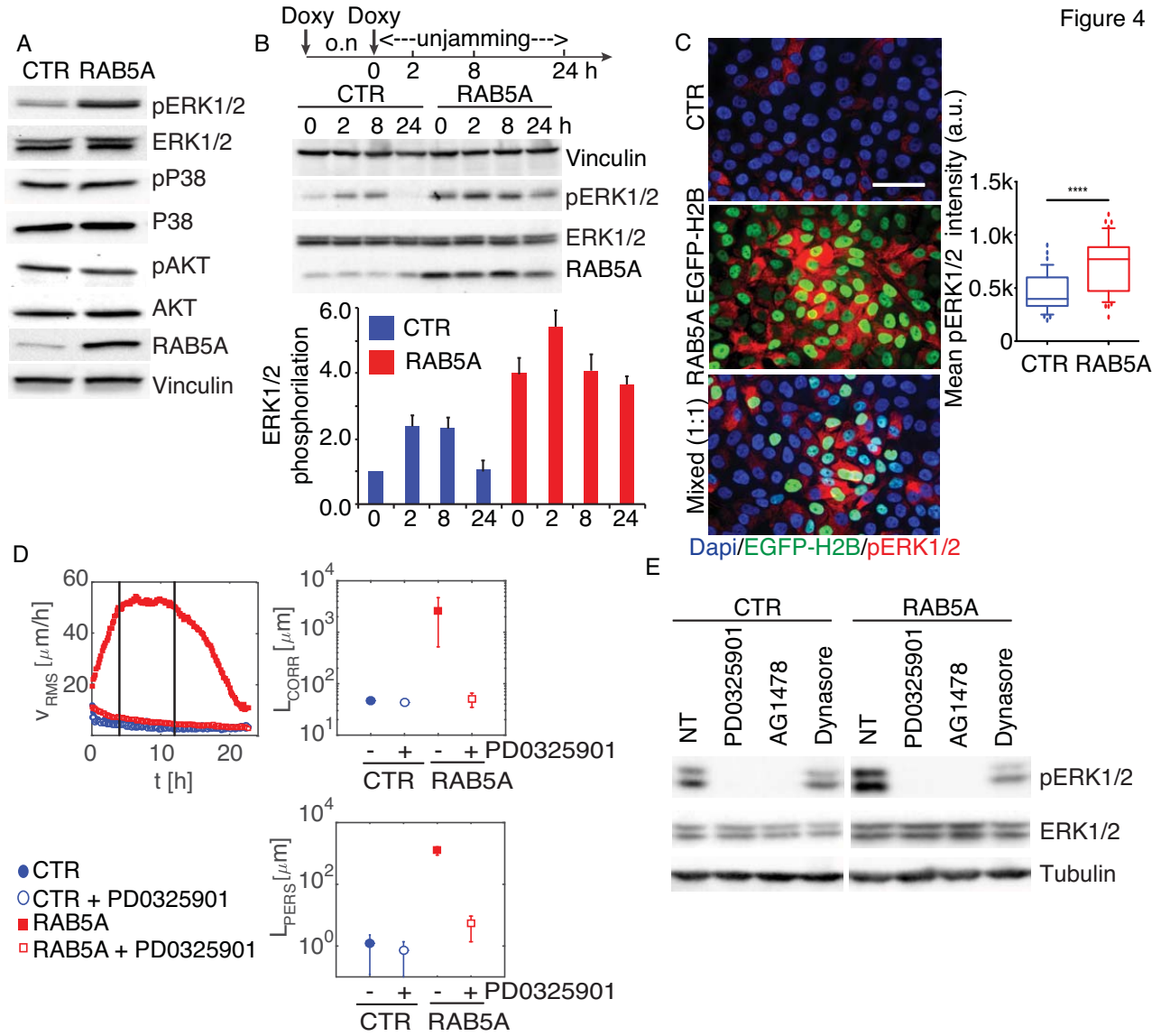
A
CTR RAB5A
pERK1/2
ERK1/2
pP38
P38
pAKT
AKT
RAB5A
Vinculin
B
Doxy Doxy
o.n
<---unjamming--->
0 2 8 24 h
CTR
RAB5A
0 2 8 24 0 2 8 24 h
Vinculin
pERK1/2
ERK1/2
RAB5A
ERK1/2 phosphorilation
6.0
4.0
2.0
0.0
CTR
RAB5A
0 2 8 24 0 2 8 24
C
CTR
RAB5A EGFP-H2B
Mixed (1:1)
Dapi/EGFP-H2B/pERK1/2
Mean pERK1/2 intensity (a.u.)
1.5k
1.0k
0.5k
0
****
CTR RAB5A
D
v_{RMS} [μm/h]
60
40
20
0 10 20
t [h]
L_{CORR} [μm]
10^4
10^3
10^2
10^1
- + - + PD0325901
CTR RAB5A
CTR
CTR + PD0325901
RAB5A
RAB5A + PD0325901
L_{PERS} [μm]
10^4
10^2
10^0
- + - + PD0325901
CTR RAB5A
E
CTR
RAB5A
NT
PD0325901
AG1478
Dynasore
NT
PD0325901
AG1478
Dynasore
pERK1/2
ERK1/2
Tubulin
F
475 nm
433 nm
FYVE domain SARA
Venus
ECFP
ERK 1/2 phospho site
WW domain
530 nm
FRET
pT
433 nm
G
CFP
Venus
EEA1
R colocalization = 0.89
Ch1 (Venus)
Ch2 (EEA1)
H
SF
PD0325901
EGF
CTR
RAB5
255
188
0
FRET efficiency
2
1.5
1
0.5
**
**
SF PD0325901 EGF
FRET efficiency
2
1.5
1
0.5
*
CTR RAB5

537 **Figure 4. RAB5A-induced, EGFR-dependent endosomal ERK1/2 activity is required for**
538 **flocking locomotion in epithelial monolayer**

539 **A**. Total cellular lysates of control and RAB5A-MCF10A cells seeded at jamming density and treated
540 with doxycycline for 16 h to induced RAB5A expression were immunoblotted with the indicated abs.
541 **B**. Total cellular lysates of control and RAB5A-MCF10A cells seeded at jamming density were
542 treated with doxycycline overnight (o.n.). The morning after, the media was replenished and cells
543 were either monitored by time lapse to follow their kinematics or lysed at various time point in order
544 to follow the phosphorylation status by immunoblotting of ERK1/2, coincidentally with the
545 expression of RAB5A and the reawakening of locomotion (not shown), as indicated in the
546 experimental scheme reported above. The ratio of phosphoERK1/2/totalERK1/2 is plotted below and
547 expressed as mean±SD (n=3 independent experiments).

548 **C**. Doxycycline-induced control and EGFP-H2B-RAB5A cells were seeded at jamming either alone
549 or mixed at a 1:1 ratio (Mixed) fixed and stained against phosphorylated ERK1/2 or processed for
550 epifluorescence. The mean±SD of the intensity of pERK1/2 is shown in the box plots (n=200 cells in
551 at 3 independent experiments). Box and whisker: 10-90 percentiles. Outliers are plotted as bubbles
552 and medias are horizontal lines in the boxes. ****$p<0.0001$. P value was calculated Student's t-test.
553 Scale Bar, 50 μm.

554 **D**. Doxycycline-treated control and RAB5A-MCF10A cells seeded at jamming density were
555 incubated with vehicle or PD0325901 (1 μM), a MEK inhibitor, 1 h before starting time-lapse
556 recording (Movie S6). PIV analysis was applied to extract: root mean square velocity v_{RMS}, plotted
557 as a function of time, correlation length L_{corr} and persistence length L_{pers}. Data are the mean±SD
558 (n=5 movies/ conditions out of 3 independent experiments).

559 **E**. Total cellular lysate of doxycycline-treated control and RAB5A-MCF10A cells seeded at jamming
560 density treated with PD0325901, or AG1478, or Dynasore (80 μg/ml) or vehicle as control were
561 immunoblotted with the indicated abs. Data are representative of 4 experiments with similar outcome.

562 **F**. Scheme of the Endo-ERK1/2-FRET sensor. The FYVE domain of SARA protein is appended at
563 the C-terminus of an EKAREV construct[56] carrying from C-terminus to the N-terminus: Venus, the
564 domain binding WW phosphopeptide, a 72-Gly linker, a ERK1/2 Serine-containing substrate (sensor
565 domain) and ECFP.

566 **G**. Endo-ERK1/2-FRET sensor localized into EEA1-positive early endosomes. Representative
567 images of Endo-ERK1/2-FRET transfected MCF10A cells stained with anti-EEA1. The extent of
568 colocalization between the Endo-ERK1/2-FRET sensor and EEA1 is shown on the right as Pearson
569 Correlation coefficient. Scale Bar, 20 μm

570 **H**. *Upper panels*, Endo-ERK1/2-FRET transfected control MCF10A cells were either serum starved
571 (SF) for 24 h or treated with PD0325901 or incubated with EGF (20ng/ml), then fixed and processed
572 for detection of FRET efficiency as described in methods. FRET efficiency normalized to control,
573 serum free MCF10A cells are the mean±SD (n=55 cells/experimental condition in three independent
574 experiments). *Bottom panels*, Endo-ERK1/2-FRET transfected control or RAB5A-MCF10A cells
575 were processed for epifluorescence as described above. FRET efficiency normalized to the value of
576 control cells is expressed as mean±SD (n=75 cells/experimental condition in 3 independent
577 experiments). Scale Bar, 20 μm

578 *$p<0.05$, ** $p<0.01$. P value were calculated using Student's t-test.

579

Figure 5

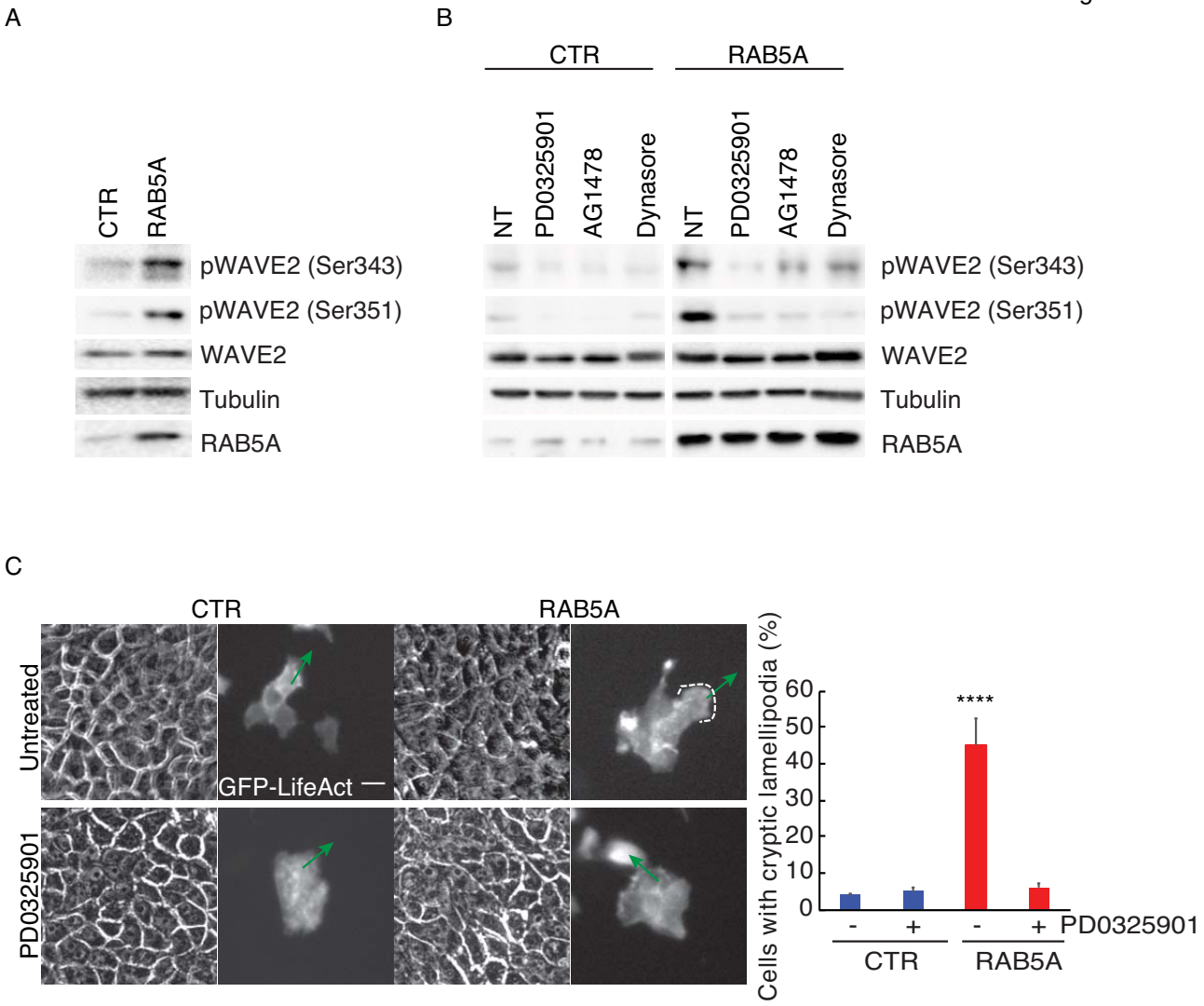

Figure 5. Endosomal ERK1/2 activation leads to phosphorylation of WAVE2, which is required for cryptic lamellipodia extension

A-B. Total cellular lysate of doxycycline-treated control and RAB5A-MCF10A cells seeded at jamming density (A) or treated (B) with either vehicle (NT) or with PD0325901, or AG1478, or Dynasore were immunoblotted with the indicated abs.

C. Still phase-contrast and fluorescent images of cryptic lamellipodia in control and RAB5A-MCF-10A monolayers composed of mosaically GFP-LifeAct-expressing (green):non-expressing cells (1:10 ratio) monitored by time-lapse microscopy (Movie S11). Green arrows indicate the orientations of protrusions. Scale bars, 20 μm. Right plot: proportion of cells with lamellipodium. Data are the mean±SD. (n=65 cells/conditions from 4 independent experiments) ****p<0.0001, Student's t-test.

Figure 6

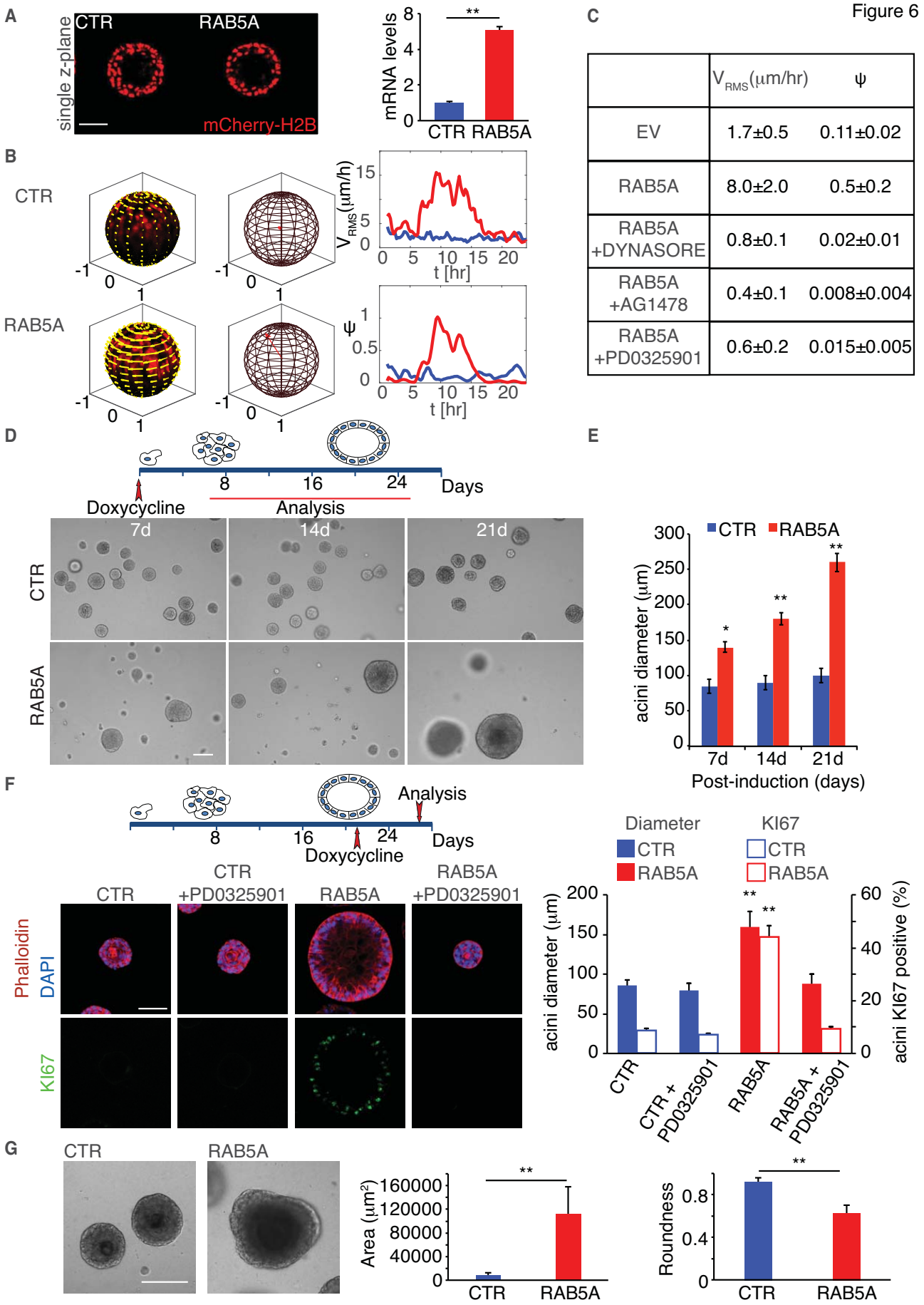

	V_{RMS}(μm/hr)	ψ
EV	1.7±0.5	0.11±0.02
RAB5A	8.0±2.0	0.5±0.2
RAB5A +DYNASORE	0.8±0.1	0.02±0.01
RAB5A +AG1478	0.4±0.1	0.008±0.004
RAB5A +PD0325901	0.6±0.2	0.015±0.005

591

592 **Figure 6. RAB5A-mediated unjamming overcomes kinetic and proliferation arrest in terminal**
593 **differentiated mammary acini.**

594 **A-B**. Control and RAB5A-MCF10A-expressing mCherry-H2B cells were grown overlaid on top of
595 Matrigel plugs. Between 14 and 21 days, cells formed fully differentiated hollow acini. At this stage,
596 Doxycycline was added and the kinematic of the 3D acini was monitored by confocal times lapse for
597 24 h (Movies S12). Representative images of single Z planes are shown. RAB5A induction was
598 verified by QRT-PCR, expressed relative to control after normalizing to GAPDH. The data are the
599 relative level of gene expression compared to control expressed as mean ± SD (n=3 independent
600 experiments). Scale Bar, 50 μm. In **B**, snapshots of the tangential velocity field at t = 10 h (indicated
601 by yellow arrows) obtained from PIV analysis are shown, overlaid on radial projection of the acini
602 onto a unit spherical surface (see also Movies S13). The direction of the red arrow shown in the
603 middle panel is parallel to the instantaneous total angular momentum $\boldsymbol{l}$ and provides the orientation
604 of the instantaneous axis of rotation, while its length is equal to the instantaneous order parameter ψ.
605 On the right: time evolution of the root mean square velocity v_{RMS} and of the rotational order
606 parameter ψ (see text and Methods for details). The data are representative of 4 movies in 3
607 independent experiments.

608 **C**. Doxycycline-treated control and RAB5A-MCF-10A mcherry-H2B- expressing MCF10A acini
609 were treated with the indicated vehicle or the indicated inhibitor and monitored by confocal time-
610 lapse microscopy for 24 hr (Movie S14). Average values of v_{RMS} and of ψ, calculated over the time
611 window comprised between 4 and 12 h, are reported. Values are from 5 movies form 3 independent
612 experiments.

613 **D-E**. Doxycycline-treated control and RAB5A-MCF10A cells were grown overlaid on top of
614 Matrigel plugs for up to 21 days. Acini were fixed and processed for phase contrast imaging to
615 monitor acini shape and size (left images) or, at various time point, for immunofluorescence to detect
616 apoptotic caspase+ and proliferating, Ki67+ cells (see Fig. S4). Exemplar, phase contrast images are

617 shown, (see also Movie S15). Scale Bar, 100 μm. In (**E**), The average size of acini was quantified
618 and expressed as mean±SD (n=100 acini/conditions in 5 independent experiments. *p<0.05, **
619 p<0.01. P value were calculated using each-pair Student's t-test.
620 **F.** Control and RAB5A-MCF10A cells were grown overlaid on top of Matrigel plugs for 14 days to
621 allow full differentiation into hollow acini. Doxycycline was then added (time schedule of drug
622 administration is on the top) to induce RAB5A expression in the presence or absence of PD0325901
623 and after 6 days acini were fixed and stained as indicated. Scale Bar, 80 μm. The size of acini was
624 calculated by measuring their diameter. The number of KI67+ acini is also reported. Data are
625 mean±SD (n=25 acini/conditions in 3 independent experiments). ** p<0.01. P value were calculated
626 using each-pair Student's t-test.
627 **G**. Doxycycline-treated control and RAB5A-MCF10A cells were grown overlaid on top of mixed
628 Matrigel:Collagene Type I (1:1) plugs for 21 days. Acini were fixed and processed for phase contrast
629 imaging to monitor acini shape and size (left images). Exemplar phase contrast images are shown.
630 Scale bar, 100 μm. Area of acini and acini roundness was quantified and expressed as mean±SD
631 (n=40 acini/conditions in 5 independent experiments). ** p<0.01, paired Student's t-test.
632

Figure 7

A

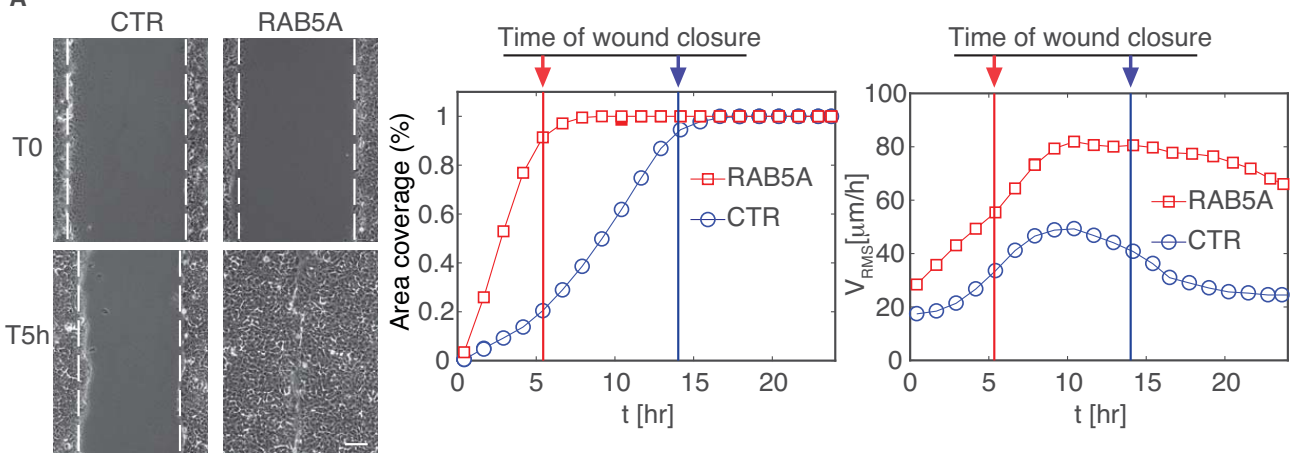

B

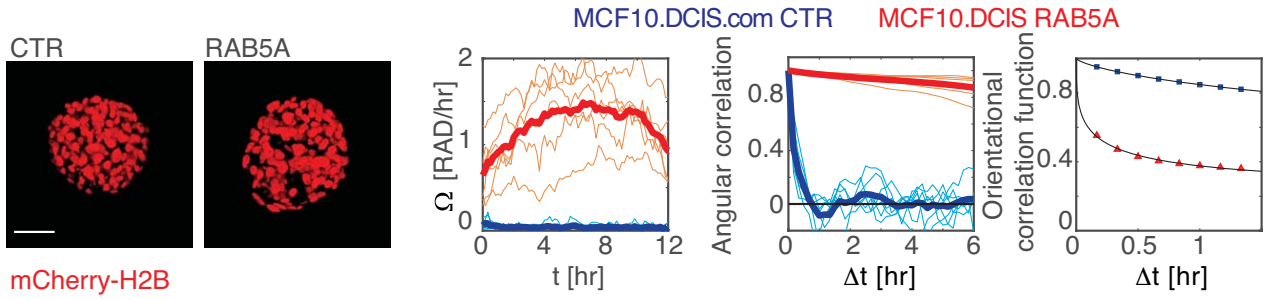

C

	Ω (rad/hr)	Correlation time (hr)
CTR	4.16×10^{-2}	1.42×10^{-1}
RAB5A	1.17	>24
RAB5A+DYNASORE	4.95×10^{-2}	7.09×10^{-1}
RAB5A+PD0325901	4.44×10^{-2}	4.98×10^{-1}
RAB5A+AG1478	5.59×10^{-2}	4.84×10^{-1}
RAB5A+CK666	3.85×10^{-2}	2.13×10^{-1}

D

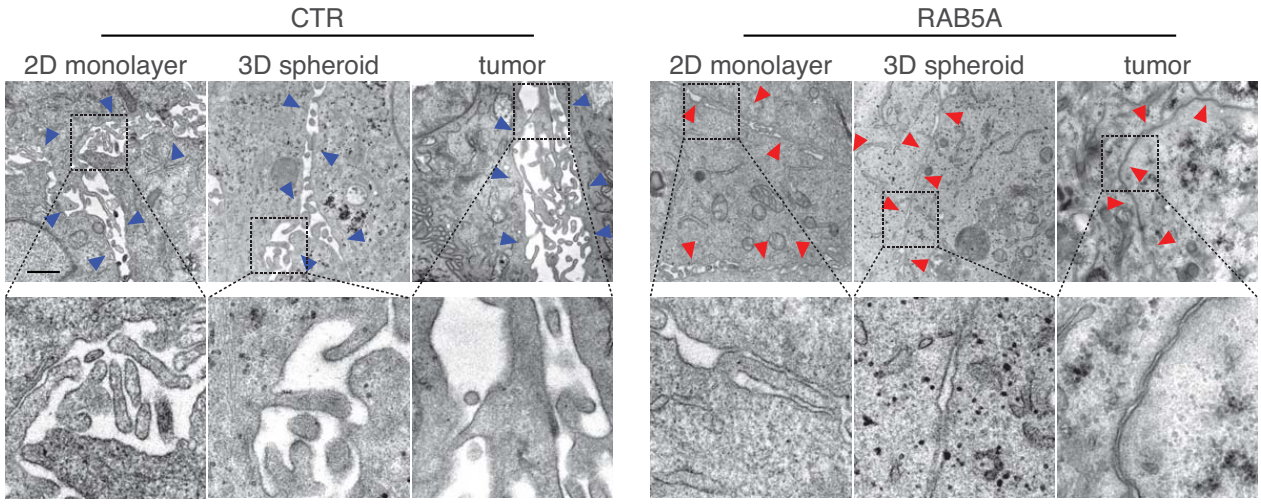

633

634 **Figure 7. RAB5A-mediated unjamming promotes the emergence of coordinated angular**
635 **rotation mode of breast cancer spheroids**

636 **A.** Scratched wound migration of doxycycline-treated control and RAB5A-MCF10.DCIS.com
637 seeded at jamming density. Representative still images at the indicated time points are shown. Dashed
638 lines mark the wound edges. Scale bar, 100 μm. Motility was quantified by measuring (left) the
639 percentage of area covered over time (calculations made with MATLABb software). On the most
640 righthand, we also quantified v_{RMS} as function of time using PIV, along the entire movies to reveal
641 that while control cells ceased migration, RAB5A-MCF10.DCIS.com keep on flowing (see Movie
642 S17). Vertical bars indicate the time at which wounds close. Data are representative of 1 experiment
643 out of >10 that were performed with similar outcome.

644 **B.** Snapshots of control and RAB5A-MCF10.DCIS.com expressing mCherry-H2B that were grown
645 as spheroids in low attachments plates. Spheroids were then embedded in thick 6.0 mg/ml of native
646 Collagen Type I gels. After addition of doxycycline, the kinematic of spheroids was monitored by
647 confocal time lapse microscopy (Movie S18). A variance-based analysis was performed to extract
648 the angular velocity Ω (expressed as rad/hr) of the spheroids as a function of time. The persistence of
649 the rotational motion is quantified by considering the decay of the orientational correlation function,
650 while the non-rigid part of the motion the spheroids, involving mutual cell rearrangement and fluid-
651 like dynamics, is captured by the so-called overlap parameter Q (see Methods for details). The
652 analysis was performed on 5-8 spheroid/conditions out of 3 independent experiments.

653 **C.** inematic parameters of doxycycline-treated control and RAB5A-MCF10.DCIS.com expressing
654 mCherry-H2B spheroids under the experimental conditions described above but treated with vehicle
655 or the various indicated inhibitors (Movie S19). Mean angular velocity Ω and correlation time,
656 extracted from an exponential fit of the orientational correlation functions, are reported (n=5
657 spheroids/condition out of 3 independent experiments).

658 **D.** Representative electron microscopy micrographs of doxycycline-treated control and RAB5A-
659 MCF10.DCIS.com cells that were seeded at jamming density as 2D monolayers, allowed to form 3D
660 spheroids which were embedded into thick, native Collagen type I gels, or injected into the mammary
661 fat pad of immune-compromised mice. Blue arrows point to large spaces between cell–cell contacts,
662 red arrows to tight cell–cell contacts. Scale bars, 2 μm.
663

Figure 8

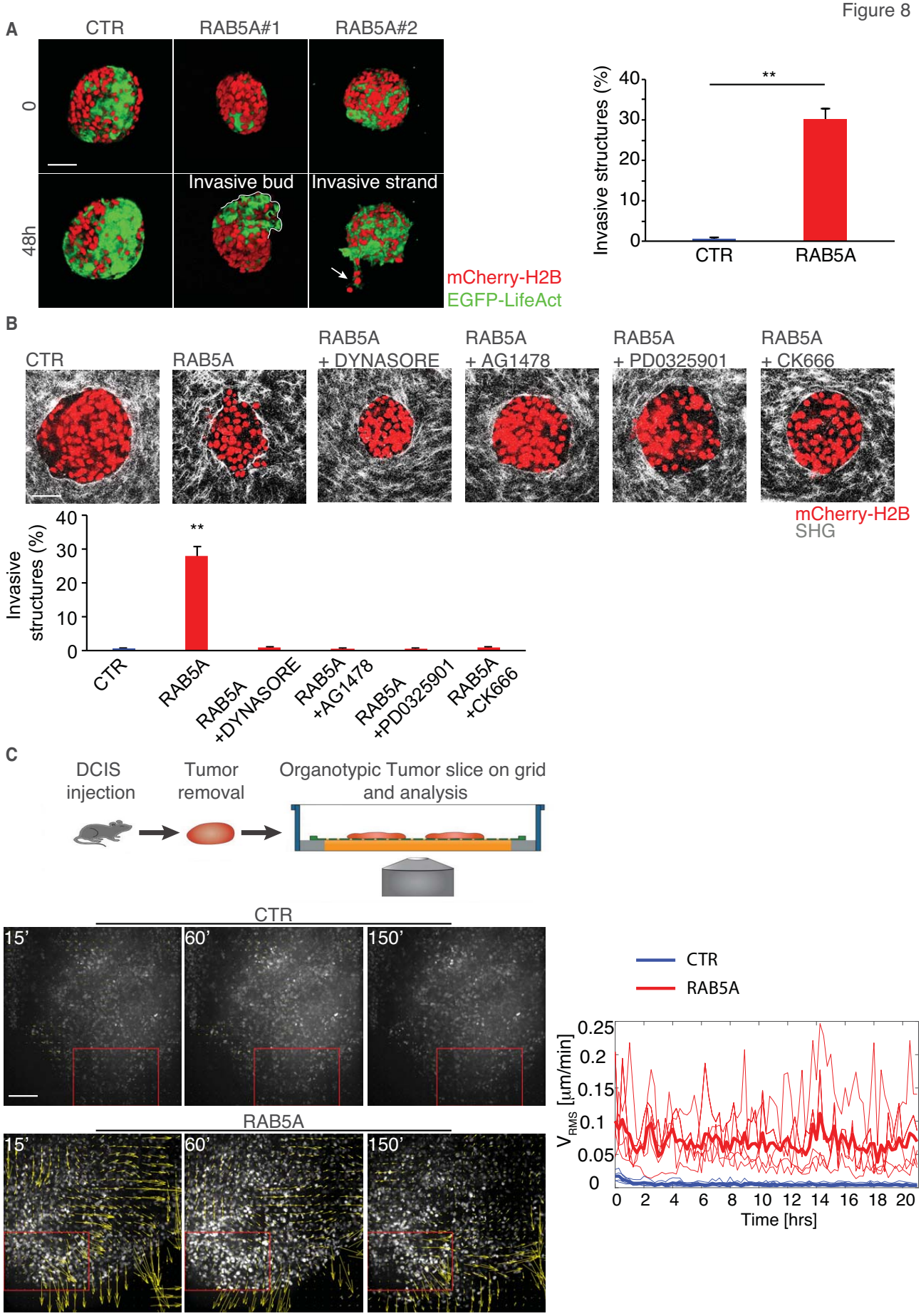
A
CTR
RAB5A#1
RAB5A#2
0
48h
Invasive bud
Invasive strand
mCherry-H2B
EGFP-LifeAct
Invasive structures (%)
40
30
20
10
0
**
CTR
RAB5A
B
CTR
RAB5A
RAB5A + DYNASORE
RAB5A + AG1478
RAB5A + PD0325901
RAB5A + CK666
mCherry-H2B
SHG
Invasive structures (%)
40
30
20
10
0
**
CTR
RAB5A
RAB5A +DYNASORE
RAB5A +AG1478
RAB5A +PD0325901
RAB5A +CK666
C
DCIS injection
Tumor removal
Organotypic Tumor slice on grid and analysis
CTR
15'
60'
150'
RAB5A
15'
60'
150'
CTR
RAB5A
V_{RMS} [µm/min]
0.25
0.2
0.15
0.1
0.05
0
0 2 4 6 8 10 12 14 16 18 20
Time [hrs]

664

665 **Figure 8 RAB5A-mediated 3D unjamming promotes collective invasion in tumour spheroids**
666 **and in ex vivo DCIS tumours slices**

667 **A**. Control and RAB5A-MCF10.DCIS.com expressing mCherry-H2B and EGFP-LifeAct were
668 grown as spheroid in low attachment. Spheroids were then embedded in thick 6.0 mg/ml of native
669 Collagen Type I gels. After addition of doxycycline, the kinematic of spheroids and the formation of
670 invasive multicellular structures was monitored by confocal time lapse microscopy and snapshots are
671 shown (Movie S20). The line delineates an invasive multicellular bud; the arrow points to an invasive
672 strand. The percentage of spheroids with invasive multicellular structures was scored and expressed
673 as mean±SD (n=15/experimental conditions in 5 independent experiments). ** $p<0.01$, calculated
674 using Student's t-test. Scale Bar, 150 μm.

675 **B.** Analysis of Collagen type I structures using SHG of doxycycline-treated Control and RAB5A-
676 MCF10.DCIS.com expressing mCherry-H2B spheroids embedded into 6.0 mg/ml of native Collagen
677 Type I gels in the presence of vehicle or the indicated inhibitors. The percentage of spheroids with
678 invasive multicellular structures was scored and expressed as mean±SD (n=15/experimental
679 conditions in 5 independent experiments). ** $p<0.01$, calculated using each-pair Student's t-test.
680 Scale Bar, 70 μm.

681 **C.** Schematic of the experimental design. Control and RAB5A-MCF10.DCIS.com expressing
682 mCherry-H2B and EGFP-LifeAct cells ($2X10^5$) were injected into the mammary fat pad of
683 immunocompromised mice. After 4 weeks, tumours that forms ductal carcinoma in situ lesion that
684 are progression to become IDC were mechanically excised and tumour tissues slices were placed on
685 a grid at the air-liquid interface. The organotypic cultures were treated with doxycycline and
686 monitored by time-lapse confocal microscopy (Movie S21) for 24hr. Snapshots of the velocity fields
687 obtained from PIV analysis of motion (Movie 22), which was used to extract the root mean square
688 velocity, $v_{RMS,}$ as function of time (Right plot). Boxed areas indicate representative fields of view used
689 for the analysis (At least 5 field of view/movies of 3 independent experiments were analysed). Thin

690 lines in the right plot indicate the actual evolution of v_{RMS}/ in each of the field of view, while thick

691 lines are the average of the v_{RMS}. Scale Bar, 150 μm.

692 **References**

693 1. Friedl, P. & Gilmour, D. Collective cell migration in morphogenesis, regeneration and cancer.
694 *Nat. Rev. Mol. Cell Biol.* **10**, 445-457 (2009).
695 2. Hakim, V. & Silberzan, P. Collective cell migration: a physics perspective. *Rep Prog Phys*
696 **80**, 076601 (2017).
697 3. Friedl, P. & Mayor, R. Tuning Collective Cell Migration by Cell-Cell Junction Regulation.
698 *Cold Spring Harbor perspectives in biology* **9** (2017).
699 4. Vedula, S.R., Ravasio, A., Lim, C.T. & Ladoux, B. Collective cell migration: a mechanistic
700 perspective. *Physiology (Bethesda)* **28**, 370-379 (2013).
701 5. Labernadie, A. & Trepat, X. Sticking, steering, squeezing and shearing: cell movements
702 driven by heterotypic mechanical forces. *Curr Opin Cell Biol* **54**, 57-65 (2018).
703 6. Park, J.A., Atia, L., Mitchel, J.A., Fredberg, J.J. & Butler, J.P. Collective migration and cell
704 jamming in asthma, cancer and development. *J Cell Sci* **129**, 3375-3383 (2016).
705 7. Bi, D., Yang, X., Marchetti, M.C. & Manning, M.L. Motility-Driven Glass and Jamming
706 Transitions in Biological Tissues. *Physical Review X* **6**, 021011 (2016).
707 8. Sadati, M., Taheri Qazvini, N., Krishnan, R., Park, C.Y. & Fredberg, J.J. Collective migration
708 and cell jamming. *Differentiation; research in biological diversity* **86**, 121-125 (2013).
709 9. Atia, L. *et al.* Geometric constraints during epithelial jamming. *Nature Physics* **14**, 613-620
710 (2018).
711 10. Oswald, L., Grosser, S., Smith, D.M. & Kas, J.A. Jamming transitions in cancer. *J Phys D*
712 *Appl Phys* **50**, 483001 (2017).
713 11. van Helvert, S., Storm, C. & Friedl, P. Mechanoreciprocity in cell migration. *Nat Cell Biol*
714 **20**, 8-20 (2018).
715 12. Haeger, A., Krause, M., Wolf, K. & Friedl, P. Cell jamming: collective invasion of
716 mesenchymal tumor cells imposed by tissue confinement. *Biochim Biophys Acta* **1840**, 2386-
717 2395 (2014).
718 13. Ye, X. & Weinberg, R.A. Epithelial-Mesenchymal Plasticity: A Central Regulator of Cancer
719 Progression. *Trends Cell Biol* **25**, 675-686 (2015).
720 14. Nieto, M.A., Huang, R.Y., Jackson, R.A. & Thiery, J.P. Emt: 2016. *Cell* **166**, 21-45 (2016).
721 15. Friedl, P., Locker, J., Sahai, E. & Segall, J.E. Classifying collective cancer cell invasion.
722 *Nature cell biology* **14**, 777-783 (2012).
723 16. Cheung, K.J. & Ewald, A.J. A collective route to metastasis: Seeding by tumor cell clusters.
724 *Science* **352**, 167-169 (2016).
725 17. Cheung, K.J. *et al.* Polyclonal breast cancer metastases arise from collective dissemination of
726 keratin 14-expressing tumor cell clusters. *Proc Natl Acad Sci U S A* **113**, E854-863 (2016).
727 18. Cheung, K.J., Gabrielson, E., Werb, Z. & Ewald, A.J. Collective invasion in breast cancer
728 requires a conserved basal epithelial program. *Cell* **155**, 1639-1651 (2013).
729 19. Aceto, N. *et al.* Circulating tumor cell clusters are oligoclonal precursors of breast cancer
730 metastasis. *Cell* **158**, 1110-1122 (2014).
731 20. Khalil, A.A. *et al.* Collective invasion in ductal and lobular breast cancer associates with
732 distant metastasis. *Clin Exp Metastasis* **34**, 421-429 (2017).
733 21. Clark, A.G. & Vignjevic, D.M. Modes of cancer cell invasion and the role of the
734 microenvironment. *Curr Opin Cell Biol* **36**, 13-22 (2015).
735 22. Hosseini, H. *et al.* Early dissemination seeds metastasis in breast cancer. *Nature* (2016).
736 23. Harper, K.L. *et al.* Mechanism of early dissemination and metastasis in Her2+ mammary
737 cancer. *Nature* (2016).

24. Scita, G. & Di Fiore, P.P. The endocytic matrix. *Nature* **463**, 464-473 (2010).
25. Sigismund, S. & Scita, G. The "endocytic matrix reloaded" and its impact on the plasticity of migratory strategies. *Curr Opin Cell Biol* **In Press** (2018).
26. Corallino, S., Malabarba, M.G., Zobel, M., Di Fiore, P.P. & Scita, G. Epithelial-to-Mesenchymal Plasticity Harnesses Endocytic Circuitries. *Frontiers in oncology* **5**, 45 (2015).
27. Chepizhko, O. *et al.* From jamming to collective cell migration through a boundary induced transition. *Soft matter* (2018).
28. Chepizhko, O. *et al.* Bursts of activity in collective cell migration. *Proc Natl Acad Sci U S A* **113**, 11408-11413 (2016).
29. Palamidessi, A. *et al.* Endocytic trafficking of Rac is required for the spatial restriction of signaling in cell migration. *Cell* **134**, 135-147 (2008).
30. Frittoli, E. *et al.* A RAB5/RAB4 recycling circuitry induces a proteolytic invasive program and promotes tumor dissemination. *J Cell Biol* **206**, 307-328 (2014).
31. Malinverno, C. *et al.* Endocytic reawakening of motility in jammed epithelia. *Nature materials* **16**, 587-596 (2017).
32. Giavazzi, F. *et al.* Giant fluctuations and structural effects in a flocking epithelium. *Journal of Physics D: Applied Physics* **50**, 384003 (2017).
33. Giavazzi, F. *et al.* Flocking transitions in confluent tissues. *Soft matter* **14**, 3471-3477 (2018).
34. Machesky, L.M. *et al.* Scar, a WASp-related protein, activates nucleation of actin filaments by the Arp2/3 complex. *Proc Natl Acad Sci U S A* **96**, 3739-3744 (1999).
35. Suetsugu, S., Miki, H. & Takenawa, T. Identification of two human WAVE/SCAR homologues as general actin regulatory molecules which associate with the Arp2/3 complex. *Biochem Biophys Res Commun* **260**, 296-302 (1999).
36. Yang, P.S. *et al.* Rab5A is associated with axillary lymph node metastasis in breast cancer patients. *Cancer Sci* **102**, 2172-2178 (2011).
37. Szabo, B. *et al.* Phase transition in the collective migration of tissue cells: experiment and model. *Phys Rev E Stat Nonlin Soft Matter Phys* **74**, 061908 (2006).
38. Debnath, J., Muthuswamy, S.K. & Brugge, J.S. Morphogenesis and oncogenesis of MCF-10A mammary epithelial acini grown in three-dimensional basement membrane cultures. *Methods* **30**, 256-268 (2003).
39. Levitzki, A. & Gazit, A. Tyrosine kinase inhibition: an approach to drug development. *Science* **267**, 1782-1788 (1995).
40. Zeigerer, A. *et al.* Rab5 is necessary for the biogenesis of the endolysosomal system in vivo. *Nature* **485**, 465-470 (2012).
41. Kirchhausen, T., Owen, D. & Harrison, S.C. Molecular structure, function, and dynamics of clathrin-mediated membrane traffic. *Cold Spring Harbor perspectives in biology* **6**, a016725 (2014).
42. Boucrot, E. *et al.* Endophilin marks and controls a clathrin-independent endocytic pathway. *Nature* **517**, 460-465 (2015).
43. Orth, J.D., Krueger, E.W., Weller, S.G. & McNiven, M.A. A novel endocytic mechanism of epidermal growth factor receptor sequestration and internalization. *Cancer Res* **66**, 3603-3610 (2006).
44. Sigismund, S. *et al.* Clathrin-mediated internalization is essential for sustained EGFR signaling but dispensable for degradation. *Dev Cell* **15**, 209-219 (2008).
45. Caldieri, G. *et al.* Reticulon 3-dependent ER-PM contact sites control EGFR nonclathrin endocytosis. *Science* **356**, 617-624 (2017).
46. Sigismund, S. *et al.* Endocytosis and signaling: cell logistics shape the eukaryotic cell plan. *Physiol Rev* **92**, 273-366 (2012).

786 47. Di Guglielmo, G.M., Baass, P.C., Ou, W.J., Posner, B.I. & Bergeron, J.J.
787 Compartmentalization of SHC, GRB2 and mSOS, and hyperphosphorylation of Raf-1 by EGF
788 but not insulin in liver parenchyma. *EMBO J* **13**, 4269-4277 (1994).
789 48. Vieira, A.V., Lamaze, C. & Schmid, S.L. Control of EGF receptor signaling by clathrin-
790 mediated endocytosis. *Science* **274**, 2086-2089 (1996).
791 49. McDonald, P.H. *et al.* Beta-arrestin 2: a receptor-regulated MAPK scaffold for the activation
792 of JNK3. *Science* **290**, 1574-1577 (2000).
793 50. Sousa, L.P. *et al.* Suppression of EGFR endocytosis by dynamin depletion reveals that EGFR
794 signaling occurs primarily at the plasma membrane. *Proc Natl Acad Sci U S A* **109**, 4419-
795 4424 (2012).
796 51. Brankatschk, B. *et al.* Regulation of the EGF transcriptional response by endocytic sorting.
797 *Science signaling* **5**, ra21 (2012).
798 52. Villasenor, R., Nonaka, H., Del Conte-Zerial, P., Kalaidzidis, Y. & Zerial, M. Regulation of
799 EGFR signal transduction by analogue-to-digital conversion in endosomes. *eLife* **4** (2015).
800 53. Matsubayashi, Y., Ebisuya, M., Honjoh, S. & Nishida, E. ERK activation propagates in
801 epithelial cell sheets and regulates their migration during wound healing. *Curr Biol* **14**, 731-
802 735 (2004).
803 54. Barrett, S.D. *et al.* The discovery of the benzhydroxamate MEK inhibitors CI-1040 and PD
804 0325901. *Bioorg Med Chem Lett* **18**, 6501-6504 (2008).
805 55. Kirchhausen, T., Macia, E. & Pelish, H.E. Use of dynasore, the small molecule inhibitor of
806 dynamin, in the regulation of endocytosis. *Methods Enzymol* **438**, 77-93 (2008).
807 56. Komatsu, N. *et al.* Development of an optimized backbone of FRET biosensors for kinases
808 and GTPases. *Mol Biol Cell* **22**, 4647-4656 (2011).
809 57. Itoh, F. *et al.* The FYVE domain in Smad anchor for receptor activation (SARA) is sufficient
810 for localization of SARA in early endosomes and regulates TGF-beta/Smad signalling. *Genes*
811 *to cells : devoted to molecular & cellular mechanisms* **7**, 321-331 (2002).
812 58. Teis, D., Wunderlich, W. & Huber, L.A. Localization of the MP1-MAPK scaffold complex
813 to endosomes is mediated by p14 and required for signal transduction. *Dev Cell* **3**, 803-814
814 (2002).
815 59. Nada, S. *et al.* The novel lipid raft adaptor p18 controls endosome dynamics by anchoring the
816 MEK-ERK pathway to late endosomes. *EMBO J* **28**, 477-489 (2009).
817 60. Farooqui, R. & Fenteany, G. Multiple rows of cells behind an epithelial wound edge extend
818 cryptic lamellipodia to collectively drive cell-sheet movement. *J Cell Sci* **118**, 51-63 (2005).
819 61. Alekhina, O., Burstein, E. & Billadeau, D.D. Cellular functions of WASP family proteins at
820 a glance. *J Cell Sci* **130**, 2235-2241 (2017).
821 62. Mendoza, M.C., Vilela, M., Juarez, J.E., Blenis, J. & Danuser, G. ERK reinforces actin
822 polymerization to power persistent edge protrusion during motility. *Science signaling* **8**, ra47
823 (2015).
824 63. Mendoza, M.C. *et al.* ERK-MAPK drives lamellipodia protrusion by activating the WAVE2
825 regulatory complex. *Mol Cell* **41**, 661-671 (2011).
826 64. Huebner, R.J., Neumann, N.M. & Ewald, A.J. Mammary epithelial tubes elongate through
827 MAPK-dependent coordination of cell migration. *Development* **143**, 983-993 (2016).
828 65. Ewald, A.J., Brenot, A., Duong, M., Chan, B.S. & Werb, Z. Collective epithelial migration
829 and cell rearrangements drive mammary branching morphogenesis. *Dev Cell* **14**, 570-581
830 (2008).
831 66. Kim, H.Y. & Nelson, C.M. Extracellular matrix and cytoskeletal dynamics during branching
832 morphogenesis. *Organogenesis* **8**, 56-64 (2012).
833 67. Carey, S.P., Martin, K.E. & Reinhart-King, C.A. Three-dimensional collagen matrix induces
834 a mechanosensitive invasive epithelial phenotype. *Scientific reports* **7**, 42088 (2017).

835 68. Chuong, C.M., Bhat, R., Widelitz, R.B. & Bissell, M.J. SnapShot: Branching Morphogenesis.
836 *Cell* **158**, 1212-1212 e1211 (2014).
837 69. Mailleux, A.A., Overholtzer, M. & Brugge, J.S. Lumen formation during mammary epithelial
838 morphogenesis: insights from in vitro and in vivo models. *Cell Cycle* **7**, 57-62 (2008).
839 70. Nguyen-Ngoc, K.V. *et al.* ECM microenvironment regulates collective migration and local
840 dissemination in normal and malignant mammary epithelium. *Proc Natl Acad Sci U S A* **109**,
841 E2595-2604 (2012).
842 71. Krause, S., Maffini, M.V., Soto, A.M. & Sonnenschein, C. A novel 3D in vitro culture model
843 to study stromal-epithelial interactions in the mammary gland. *Tissue Eng Part C Methods*
844 **14**, 261-271 (2008).
845 72. Pearson, G.W. & Hunter, T. PI-3 kinase activity is necessary for ERK1/2-induced disruption
846 of mammary epithelial architecture. *Breast Cancer Res* **11**, R29 (2009).
847 73. Miller, F.R., Santner, S.J., Tait, L. & Dawson, P.J. MCF10DCIS.com xenograft model of
848 human comedo ductal carcinoma in situ. *Journal of the National Cancer Institute* **92**, 1185-
849 1186 (2000).
850 74. Dvorak, H.F. Tumors: wounds that do not heal. Similarities between tumor stroma generation
851 and wound healing. *N Engl J Med* **315**, 1650-1659 (1986).
852 75. Hu, M. & Polyak, K. Molecular characterisation of the tumour microenvironment in breast
853 cancer. *European journal of cancer* **44**, 2760-2765 (2008).
854 76. Staneva, R., Barbazan, J., Simon, A., Vignjevic, D.M. & Krndija, D. Cell Migration in
855 Tissues: Explant Culture and Live Imaging. *Methods Mol Biol* **1749**, 163-173 (2018).
856 77. Di Fiore, P.P. & von Zastrow, M. Endocytosis, signaling, and beyond. *Cold Spring Harbor*
857 *perspectives in biology* **6** (2014).
858 78. Das, T. *et al.* A molecular mechanotransduction pathway regulates collective migration of
859 epithelial cells. *Nat Cell Biol* **17**, 276-287 (2015).
860 79. Park, J.A. *et al.* Unjamming and cell shape in the asthmatic airway epithelium. *Nature*
861 *materials* **14**, 1040-1048 (2015).
862 80. Tambe, D.T. *et al.* Collective cell guidance by cooperative intercellular forces. *Nature*
863 *materials* **10**, 469-475 (2011).
864 81. Zehnder, S.M., Suaris, M., Bellaire, M.M. & Angelini, T.E. Cell Volume Fluctuations in
865 MDCK Monolayers. *Biophys J* **108**, 247-250 (2015).
866 82. Joraku, A., Sullivan, C.A., Yoo, J. & Atala, A. In-vitro reconstitution of three-dimensional
867 human salivary gland tissue structures. *Differentiation; research in biological diversity* **75**,
868 318-324 (2007).
869 83. Dang, T.T., Esparza, M.A., Maine, E.A., Westcott, J.M. & Pearson, G.W. DeltaNp63alpha
870 Promotes Breast Cancer Cell Motility through the Selective Activation of Components of the
871 Epithelial-to-Mesenchymal Transition Program. *Cancer Res* **75**, 3925-3935 (2015).
872
873

874 **METHODS**
875

876 **Plasmids, antibodies and reagents.**

877 Doxycycline-inducible lentiviral vectors pSLIK-neomycin (neo) carrying RAB5A or RAB5C
878 sequences and pSLIK-hygromycin (hygro) carrying RAB5B sequence were obtained by Gataway
879 Technology (Invitrogen), following the manufacturer's protocol. The plasmids pBABE-puromycin
880 (puro)-mCHERRY-H2B and pBABE- puro-EGFP-H2B were provided by IFOM-Imaging Facility.
881 The lentiviral expression construct pRRL-Lifeact-EGFP-puromicin (puro) was a gift of Olivier Pertz
882 (University of Basel, Basel, Switzerland). pBabe-Puro-MEK-S218D/S222D (MEK-DD) vector was
883 purchased from Addgene.
884 FRET EKAREV-ERK1/2 sensor[1] was generated by cloning synthetized FYVE domain of SARA into
885 the BamHI/EcoRI cleaved EKAREV-FRET vector to generate pPBbsr2-3560NES-EKAREV-FRET
886 new vector.
887 Mouse monoclonal antibodies raised against α−tubulin (#T5168) or vinculin (#V9131) were from
888 Sigma-Aldrich. Rabbit polyclonal anti-RAB5A (S-19, #sc-309) and goat polyclonal anti-EEA-1 (N-
889 19, #sc-6415) antibodies from Santa Cruz Biotechnology. Monoclonal rabbit anti-human RAB5A -
890 ab109534, dilution 1:100, (Abcam[EPR5438]) was used of IHC;Rabbit polyclonal anti-Giantin
891 (#PRB-114C) antibody was from Covance. Mouse monoclonal anti-human Ki-67 Antigen (MIB-1,
892 #M7240) antibody was from Dako. Mouse monoclonal anti-AP50 (AP2mu) (31/AP50, #611350) was
893 from BD Bioscience. Mouse monoclonal anti-E-cadherin (#610181) antibody was from Transduction
894 Lab. Rabbit polyclonal anti-phospho-EGFR (Tyr1086, #2220), rabbit monoclonal anti-phospho-
895 p44/42 MAPK (ERK1/2) (Thr202/Tyr204, #4370), rabbit polyclonal anti-p44/42 MAPK (ERK1/2)
896 (#9102), rabbit monoclonal anti-phospho-p38 MAPK (Thr180/Tyr182, 3D7, #9215), mouse
897 monoclonal anti-p38 MAPK (L53F8, #9228), rabbit monoclonal anti-phospho-AKT (Ser473,
898 193H12, #4058), rabbit polyclonal anti-AKT (#9272), rabbit polyclonal anti-MEK1/2 (#9122) and
899 rabbit polyclonal anti-cleaved Caspase-3 (Asp175, #9661) antibodies were from Cell Signalling

900 Technology. Rabbit polyclonal anti-phospho-WAVE2 (Ser343, #07-1512), rabbit polyclonal anti-
901 phospho-WAVE2 (Ser351, #07-1514) and mouse monoclonal anti-Laminin-V (P3H9-2,
902 #MAB1947) antibodies were from Merck/Millipore. Mouse monoclonal anti-WAVE2 antibody was
903 homemade. Rabbit polyclonal anti EGFR (806), directed against aa 1172-1186 of human EGFR
904 (ImmunoBlot) and mouse monoclonal anti-EGFR (m108 hybridoma) directed against the
905 extracellular domain of human EGFR (IF) were a gift from P.P. Di Fiore. Secondary antibodies
906 conjugated to horseradish peroxidase were from Bio-Rad (#7074, #7076); Cy3-secondary antibodies
907 from Jackson ImmunoResearch (#711-165-152, #715-165-150); DAPI (#D-1306) and AlexaFluor
908 488 (A-11055, A-21202) were from Thermo Fisher Scientific. TRITC- (#P1951) and FITC-(#P5282)
909 conjugated phalloidin were from Sigma Aldrich.
910 Doxycycline Hyclate (DOX, #D9891), Dynasore Hydrate (#D7693), AG1478 (#T4182) and CK666
911 (#SML0006) were from Sigma Aldrich. PD0325901 (#444966) was from Merck/Millipore.
912
913 **Cell cultures and transfection.**
914 MCF10A cells were a kind gift of J. S. Brugge (Department of Cell Biology, Harvard Medical School,
915 Boston, USA) and were maintained in Dulbecco's Modified Eagle Medium: Nutrient Mixture F-12
916 (DMEM/F12) medium (Biowest) supplemented with 5% horse serum, 1% L-Glutamine (EuroClone),
917 0.5 mg ml^{-1}hydrocortisone (Sigma-Aldrich), 100 ng ml^{-1} cholera toxin (Sigma-Aldrich),
918 10 μg ml^{-1} insulin (Sigma-Aldrich) and 20 ng ml^{-1} EGF (Vinci Biochem). MCF10.DCIS.com cells
919 were kindly provided by J. F. Marshall (Barts Cancer Institute, Queen Mary University of London,
920 UK) and maintained in Dulbecco's Modified Eagle Medium: Nutrient Mixture F-12 (DMEM/F12)
921 medium supplemented with 5% horse serum, 1% L-Glutamine, 0.5 mg ml^{-1}hydrocortisone,
922 10 μg ml^{-1} insulin and 20 ng ml^{-1} EGF. All cell lines have been authenticated by cell fingerprinting
923 and tested for mycoplasma contamination. Cells were grown at 37 °C in humidified atmosphere with
924 5% CO_2. MCF10A cells were infected with pSLIK-neo-EV (empty vector-CTR), pSLIK-neo-

925 RAB5A, pSLIK-hygro-RAB5B or pSLIK-neo-RAB5C lentiviruses and selected with the appropriate
926 antibiotic to obtain stable inducible cell lines. MCF10.DCIS.com were infected with pSLIK-neo-EV
927 (empty vector-CTR) or pSLIK-neo-RAB5A lentiviruses and selected with the appropriate antibiotic
928 to obtain stable inducible cell lines. Constitutive expression of EGFP-LifeAct- or mCHERRY- or
929 EGFP-H2B was achieved by lentiviral and retroviral infection of MCF10A and MCF10DCIS.com
930 cells with EGFP-LifeAct- puro or pBABE- puro-mCHERRY-H2B/ pBABE- puro-EGFP-H2B
931 vectors, respectively.
932 Transfections were performed using either calcium phosphate or FUGENE HD Transfection reagent
933 (#E2311, PROMEGA) reagents, according to manufacturer's instructions. FUGENE HD reagent was
934 used for FRET-EKAREV-ERK1/2 transfection in MCF10A cells.
935
936 **Generation of lentiviral and retroviral particles**
937 Packaging of lentiviruses or retroviruses was performed following standard protocols. Viral
938 supernatants were collected and filtered through 0.45 μm filters. Cells were subjected to four cycles
939 of infection and selected using the appropriate antibiotic: neomycin for pSLIK-neo vector (150
940 μg/ml), hygromycin for pSLIK-hygro vector (100 μg/ml) or puromycin for EGFP-LifeAct or pBABE
941 vectors (2 μg/ml). After several passages, stable bulk populations were selected and induced by
942 Doxycycline Hyclate (2.5 μg/ml) in order to test: i) induction efficiency by Western Blotting and
943 quantitative RT-PCR (qRT-PCR), and ii) the homogeneity of the cell pool by immunofluorescence
944 staining, as previously shown[2].
945
946 **RNA interference**
947 siRNAs (small interfering RNAs) delivery was achieved by mixing 1 nM of specific siRNAs with
948 Optimem and Lipofectamine RNAiMAX Transfection Reagent (Life Technologies). The first cycle
949 of interference (reverse transfection) was performed on cells in suspension. The day after, a second

950 cycle of interference (forward transfection) was performed on cells in adhesion. The following
951 siRNAs were used for knocking down specific genes. All sequences are 5' to 3'.
952 Dynamin2 (DNM2): 5'-GACATGATCCTGCAGTTCA-3' (Dharmacon)
953 AP2mu: 5'-UGACCCGAAAGGCAUCCACCCCC-3' (Riboxx)
954 MP1 (LAMTOR3): 5'-CAAUUUAAUCGUUUACCUU-3' (Silencer Select, Ambion)
955 P14 (LAMTOR2): 5'-CCCAAGUGGCGGCAUCUUA-3' (Silencer Select, Ambion)
956 Reticulon 3 (RTN3): 5'-CCCUGAAACUCAUUAUUCGUCUCUU-3' (Stealth, Invitrogen)
957 Reticulon 4 (RTN4): 5'-CCAGCCUAUUCCUGCUGCUUUCAUU-3' (Stealth, Invitrogen)
958 For each RNA interference experiment, negative control was performed with the same amount of
959 scrambled siRNAs. Silencing efficiency was controlled by qRT-PCR.
960

961 **Quantitative RT-PCR analysis**

962 Quantitative RT-PCR analysis was performed as previously shown[2]. Total RNA was extracted using
963 RNeasy Mini kit (Qiagen) and quantified by NanoDrop to assess both concentration and quality of
964 the samples. Reverse transcription was performed using SuperScript VILO cDNA Synthesis kit from
965 Invitrogen. Gene expression was analyzed using TaqMan Gene expression Assay (Applied
966 Biosystems). 0.1 ng of cDNA was amplified, in triplicate, in a reaction volume of 25 µl with 10 pMol
967 of each gene- specific primer and the SYBR-green PCR MasterMix (Applied Biosystems). Real-time
968 PCR was performed on the 14 ABI/Prism 7700 Sequence Detector System (PerkinElmer/Applied
969 Biosystems), using a pre-PCR step of 10 min at 95°C, followed by 40 cycles of 15 s at 95°C and 60
970 s at 60°C. Specificity of the amplified products was confirmed by melting curve analysis
971 (Dissociation Curve TM; PerkinElmer/Applied Biosystems) and by 6% PAGE. Preparations with
972 RNA template without reverse transcription were used as negative controls. Samples were amplified
973 with primers for each gene (for details see the Q-PCR primer list below) and GAPDH as a
974 housekeeping gene. The Ct values were normalized to the GAPDH curve. PCR experiments were

975 performed in triplicate and standard deviations calculated and displayed as error bars. Primer assay
976 IDs were: GAPDH, Hs99999905_m1; RAB5A, Hs00702360_s1; RAB5B, Hs00161184_m1 and
977 RAB5C, Hs00428044_m1, Dynamin2 (DNM2) Hs00974698_m1, MP1 (LAMTOR3)
978 Hs00179753_m1, P14 (LAMTOR2) Hs00203981_m1, Reticulon3 (RTN3) Hs01581965_m1,
979 Reticulon4 (RTN4) Hs01103689_m1.
980

981 **Immunoblotting**

982 For protein extraction, cells, previously washed with cold PBS, were lysed in JS buffer supplemented
983 with proteases and phosphatases inhibitors [50 mM HEPES PH 7.5, 50 mM NaCl, 1% glycerol; 1%
984 Triton X-100, 1.5 mM $MgCl_2$. 5 mM EGTA plus protease inhibitor cocktail (Roche, Basel,
985 Switzerland), 1 mM DTT, 20 mM Na pyrophosphate pH 7.5, 50 mM NaF, 0.5 M Na-vanadate in
986 HEPES pH 7.5 to inhibit phosphatases]. Lysates were incubated on ice for 10 minutes and cleared by
987 centrifugation at 13,000 rpm for 30 min at 4°C. Protein concentration was quantified by Bradford
988 colorimetric protein assay. The same amount of protein lysates was loaded onto polyacrylamide gel
989 in 5X SDS sample buffer. Proteins were transferred onto Protran Nitrocellulose Transfer membrane
990 (Whatman), probed with the appropriate antibodies and visualized with ECL western blotting
991 detection reagents (GE Healthcare). Membrane blocking and incubation in primary or secondary
992 antibodies were performed for 1h in TBS/0.1% Tween/5% milk for antibodies recognizing the total
993 proteins or in TBS/0.1% Tween/5% BSA for antibodies recognizing phosphorylated proteins.
994

995 **Immunohistochemistry on DCIS and IDC**

996 Sections from archival human breast cancer samples were collected from the archives of the Tumor
997 Immunology Laboratory of the Human Pathology Section, Department of Health Sciences,
998 University of Palermo, Italy.

999 Immunohistochemistry was performed using a polymer detection method (Novolink Polymer
1000 Detection Systems Novocastra, Leica Biosystems, Newcastle, Product No: RE7280-K).
1001 Tissue samples were fixed in 10% buffered formalin and embedded in paraffin. Four-micrometers-
1002 thick tissue sections were dewaxed and rehydrated. The antigen unmasking technique was performed
1003 using Novocastra Epitope Retrieval Solution pH6 citrate-based buffer in thermostatic water bath at
1004 98°C for 30 minutes. Subsequently, the sections were brought to room temperature and washed in
1005 PBS-Tween. After neutralization of the endogenous peroxidase with 3% H_2O_2 and protein blocking
1006 by a specific protein block, the samples were incubated 1h with monoclonal rabbit anti-human
1007 RAB5A [EPR5438] - ab109534 (dilution 1:100, Abcam). Staining was revealed by polymer detection
1008 kit (Novocastra, Ltd) and AEC (3-Amino-9-Ethylcarbazole) substrate chromogen. The slides were
1009 counterstained with Harris hematoxylin (Novocastra, Ltd). All the sections were analyzed under a
1010 Zeiss Axio Scope A1 optical microscope (Zeiss, Germany) and microphotographs were collected
1011 using an Axiocam 503 Color digital camera with the ZEN2 imaging software (Zeiss Germany)
1012

1013 **Cell streaming and wound healing assays**

1014 As previously shown[2], cells were seeded in 6-well plate ($1.5*10^6$ cells/well) in complete medium and
1015 cultured until a uniform monolayer had formed. RAB5A expression was induced, were indicated, 16
1016 hours before performing the experiment by adding fresh complete media supplemented with 2.5
1017 µg/ml Doxycycline Hyclate to cells. Comparable cell confluence was tested by taking pictures by
1018 differential interference contrast (DIC) imaging using a 10x objective and counting the number of
1019 nuclei/field. In cell streaming assay, medium has been refreshed before starting imaging. In wound
1020 healing assay, cells monolayer was scratched with a pipette tip and carefully washed with 1X PBS to
1021 remove floating cells and create a cell-free wound area. The closure of the wound was monitored by
1022 time-lapse. Olympus ScanR inverted microscope with 10x objective was used to take pictures every
1023 5-10 minutes over a 24 hours period (as indicated in the figure legends). The assay was performed

1024 using an environmental microscope incubator set to 37°C and 5% CO2 perfusion. After cell induction,
1025 Doxycycline Hyclate was maintained in the media for the total duration of the time-lapse experiment.
1026 The percentage of area covered by cells (area coverage %) overtime and wound front speed were
1027 calculated by MatLab software. In chemical inhibitors experiments, the inhibitor was added together
1028 with Doxycycline Hyclate in fresh media 1 h before starting imaging. For cell streaming assay
1029 performed on interfered cells, cells were interfered in suspension (first cycle) and directly plated at
1030 the desired concentration, following the same conditions already described in "RNA interference"
1031 section.
1032 For detection of cryptic lamellipodia, MCF10A cells stably expressing EGFP-LifeAct were mixed in
1033 a 1:10 ratio with unlabeled cells and seeded in cell streaming assay, as described before. Cell
1034 migration was monitored by time-lapse phase contrast and fluorescence microscopy, collecting
1035 images at multiple stage positions in each time loop. Olympus ScanR inverted microscope with 20x
1036 objective (+1.6x Optovar) was used to take pictures every 90 seconds. Each assay was done 5 times
1037 and at least 25 cells/condition were counted in each experiment. Where indicated, PD0325901 was
1038 added 1 h before imaging.
1039
1040 **FRET Analysis**
1041 Using a customised macro in ImageJ, FRET data were analysed using the ratiometric approach. CFP,
1042 YFP and FRET images were background subtracted, converted in 32bits and the smoothed YFP
1043 image were tresholded and used as a mask to highlight the vesicular-like structures of interest. On
1044 these areas the average FRET/CFP ratio was then calculated as described in Kardash E. et al. [3]
1045
1046 **3D morphogenesis assay**
1047 MCF10A morphogenesis assay was per formed as already described[67]. Briefly, MCF10A cells were
1048 trypsinized and resuspended in MCF10A culture medium. Eight-well chamber slides (#80826 IBIDI)

1049 were coated with 40 µl/well of Growth Factor Reduced Matrigel Matrix Basement Membrane HC
1050 10.2 mg/ml (#354263, Corning) or with 1:1 mixture of Matrigel HC 10.2 mg/ml and Type I Bovine
1051 Collagen 3 mg/ml (#5005 Advanced BioMatrix). Once the matrix is polymerized, $2.5*10^3$ cells were
1052 plated into each well on the top of the matrix layer in culture medium supplemented with 2% Matrigel
1053 HC 10.2 mg/ml and 5 ng/ml EGF. Complete acini morphogenesis was allowed by incubating the cells
1054 for 3 weeks and replacing assay media every four days.
1055 On day 21 acini were treated with 2.5 µg/ml Doxycycline Hyclate to induce RAB5A expression.
1056 Cells were maintained under stimulation for 6 days, changing the medium every 2 days, before
1057 fixation with 4% paraformaldehyde (PFA) and stained with specific antibodies. When inhibitors were
1058 used, the media were refreshed every day.
1059

1060 **3D spheroid kinematic assay**

1061 MCF10DCIS.com cells were plated on Ultra-Low attachment surface 6-well plate (#3471
1062 CORNING) at a density of $5*10^3$ cells/well. Cells were grown in serum-free condition for 10 days
1063 by adding fresh culture media every 2 days. Then every single well of spheres were collected and
1064 resuspended in 150 µl of 6 mg/ml Collagen Type I (#35429 CORNING), diluted in culture media, 50
1065 mM Hepes, 0,12 $NaHCO_3$ and 5 mM NaOH. The unpolymerized mix sphere/collagen was placed in
1066 Eight-well chamber slides and incubated at 37°C for o/n. The day after, before imaging, 2.5µg/ml
1067 Doxycycline Hyclate was added over the polymerized collagen mix to induce RAB5A expression.
1068

1069 **Ex Vivo DCIS tumor slice motility assay**

1070 All animal experiments were approved by the OPBA (Organisms for the well-being of the animal) of
1071 IFOM and Cogentech. All experiments complied with national guidelines and legislation for animal
1072 experimentation. All mice were bred and maintained under specific pathogen-free conditions in our
1073 animal facilities at Cogentech Consortium at the FIRC Institute of Molecular Oncology Foundation

1074 and at the European Institute of Oncology in Milan, under the authorization from the Italian Ministry
1075 of Health (Autorizzazione N° 604-2016).
1076
1077 For mammary fat pad tumor development in NSG mice MCF10DCIS.com cells were trypsin
1078 detached, washed twice, and resuspended in PBS to a final concentration $2*10^5$/13 µl. The cell
1079 suspension was then mixed with 5 µl growth factor–reduced Matrigel and 2 µl Trypan blue solution
1080 and maintained on ice until injection. Aseptic conditions under a laminar flow hood were used
1081 throughout the surgical procedure. Female NOD.Cg-PrkdcscidIl2rgtm1Wjl/SzJ (commonly known
1082 as the NOD SCID gamma; NSG) mice, 6–9 weeks old, were anesthetized with 375 mg/Kg Avertin,
1083 laid on their backs, and injected with a 20-µl cell suspension directly in the fourth mammary fad pad.
1084 After 4 weeks mice were sacrificed and the primary tumors were removed, cut by a scalpel and each
1085 tumor slide was placed over a metal grid inserted in 6-well plate to allow tumors to grow on an
1086 interface air/culture medium. Before imaging, 2.5µg/ml Doxycycline Hyclate was added to tumor
1087 slices culture media to induce RAB5A expression. Tumor cells were maintained under stimulation
1088 for 3 days, changing the medium every day.
1089
1090 **Immunofluorescence**
1091 As previously shown[2], cells were fixed in 4% paraformaldehyde (PFA) and permeabilized with 0.1%
1092 Triton X-100 and 1% BSA 10 minutes (except for EEA-1 staining, permeabilized with 0.02%
1093 Saponin and 1% BSA 10 minutes and pERK1/2 staining, permeabilized with ice cold 100% Methanol
1094 for 10 minutes). In EGFR staining experiments, permeabilization step was avoided where indicated
1095 (non-permeabilized conditions) in order to detect only total cell surface EGFR. After 1X PBS wash,
1096 primary antibodies were added for 1 hour at room temperature. Coverslips were washed in 1X PBS
1097 before secondary antibody incubation 1 hour at room temperature, protected from light. FITC- or
1098 TRITC-phalloidin was added in the secondary antibody step, where applicable. After removal of not

1099 specifically bound antibodies by 1X PBS washing, nuclei were stained with 0.5 ng/ml DAPI. Samples
1100 were post-fixed and mounted on glass slides in anti-fade mounting medium (Mowiol). Antibodies
1101 were diluted in 1X PBS and 1% BSA. Images were acquired by wide-field fluorescence microscope
1102 or confocal microscope, as indicated in figure legends.
1103 Immunofluorescence on MCF10A-derived acini was performed by fixing acini with 4%
1104 paraformaldehyde for 20 minutes at RT. Then cells were permeabilized with 0.5% TRITON X-100
1105 in PBS for 10 minutes at 4ºC and incubated with blocking solution (PBS + 0.1% BSA + 10% goat
1106 serum) for 1 hour at RT. Acini were incubated with indicated primary antibodies diluted in blocking
1107 solution for o/n at 4ºC. The day after acini were incubated with indicated secondary antibodies diluted
1108 in blocking solution for 1 hour at RT. Finally, acini were incubated with DAPI in PBS for 20 minutes
1109 at RT. Samples were then maintained at 4ºC in PBS before imaging.
1110 E-cadherin staining was analysed by confocal microscopy and images were processed to obtain the
1111 straightness index of the junction. "Junction length" was measured by tracking a straight line and
1112 "junction tracking" was obtained by tracking manually the same junction following its profile. The
1113 straightness index of the junction has been quantified as the ratio of the junction length and the
1114 junction tracking.
1115

1116 **^{125}I-EGF internalization assay**

1117 Internalization of ^{125}I-EGF was performed at low EGF (1 ng/ml) or high EGF (30 ng/ml) as described
1118 in ref.[4].
1119 Briefly, MCF10A cells were plated in 24-well plates in at least duplicate for each time point, plus
1120 one well to assess non-specific binding. Cell monolayers were EGF-starved 24 hours and induced
1121 overnight by Doxycycline Hyclate. The day after cells were incubated in assay medium (DMEM/F12
1122 supplemented with Cholera Toxin (100 ng/ml), 0,1% BSA, 20mM Hepes, DOX (2.5µg/ml) and then
1123 incubated at 37°C in the presence of 1 ng/ml ^{125}I-EGF, or 30 ng/ml EGF (1 ng/ml ^{125}I-EGF (Perkin

1124 Elmer) + 29 ng/ml cold EGF. At different time points (2, 4, 6 min) the amount of bound ^{125}I-EGF
1125 was measured with an acid wash solution pH 2.5 (0.2 M acetic acid, 0.5 M NaCl). Cells were then
1126 lysed with 1N NaOH, which represents the amount of internalized ^{125}I-EGF. Non-specific binding
1127 was measured at each time point in the presence of an excess of non-radioactive EGF (300 times).
1128 After being corrected for non-specific binding, the rate of internalisation was calculated as the ratio
1129 between internalised and surface-bound radioactivity. Surface EGFRs were measured by ^{125}I-EGF
1130 saturation binding as described[5].
1131
1132 **EGF recycling assay**
1133 Recycling assays of ^{125}I-EGF were performed as described in[5]. In brief, cell monolayers were EGF-
1134 starved 24 hours and induced overnight by Doxycycline Hyclate. The day after cells were incubated
1135 in assay medium (DMEM/F12 supplemented with Cholera Toxin (100ng/ml) , 0,1% BSA, 20mM
1136 Hepes, DOX (2.5µg/ml), then incubated with ^{125}I-EGF (30 ng/ml: 5 ng/ml of ^{125}I-EGF + 25 ng/ml of
1137 cold EGF) for 15 min at 37 °C, followed by mild acid/salt treatment (buffer at pH 4.5, 0.2 M Na
1138 acetate pH 4.5, 0.5 M NaCl) to remove bound EGF. Cells were then chased at 37°C in a medium
1139 containing 4 µg/ml EGF for the indicated times, to allow internalization and recycling. At the end of
1140 each chase time, the medium was collected, half was counted directly (free) and half was subjected
1141 to TCA precipitation to determine the amount of intact/recycled (TCA precipitable) and degraded
1142 (TCA soluble) ^{125}I-EGF present in it. Surface-bound ^{125}I-EGF was extracted by acid treatment (0.5M
1143 NaCl, 0.2M acid acetic). Finally, cells were lysed in 1N NaOH to determine intracellular ^{125}I-EGF.
1144 Data are expressed as the fraction of intact ^{125}I-EGF in the medium with respect to the total (total
1145 medium + total surface + total intracellular). Non-specific counts were measured for each time point
1146 in the presence of a 300-fold excess of cold ligand, and were never >3-10 % of the total counts.
1147
1148 **Image acquisition**

1149 Time-lapse imaging of 3D acini/spheroids motility was performed on a Leica TCS SP8 laser confocal
1150 scanner mounted on a Leica DMi8 microscope equipped with motorized stage; a HC PL FLUOTAR
1151 20X/0.5NA dry objective was used. A white light laser was used as illumination source. LAS X was
1152 the software used for all the acquisitions.
1153 Image acquisition conditions were set to remove channel crosstalk, optimizing spectral detection
1154 bands and scanning modalities. ImageJ software was used for data analysis.
1155 Collagen SHG analysis on collagen embedded MCF10DCIS spheroids was performed with a
1156 confocal microscope (Leica; TCS SP5) on an upright microscope (DM6000 CFS) equipped with blue
1157 (argon, 488 nm), yellow (561 nm solid state laser), and red (633 nm solid state laser) excitation laser
1158 lines with an HCX PL APO 40X/1.25-0.75NA oil immersion objective and controlled by Leica LAS
1159 AF software (Leica). We used a two-photon excitation (2PE) technique with a pulsed infrared laser
1160 (Chameleon Ultra II; Coherent) at 980 nm.
1161 EKAREV FRET analysis was performed using a DeltaVision Elite imaging system (Applied
1162 Precision) controlled by softWoRx Explorer 2.0 (Applied Precision) equipped with a DV Elite CMOS
1163 camera and an inverted microscope (IX71; Olympus) using a PlanApo N 60X/1.42NA oil-immersion
1164 objective lens.
1165 Ex vivo DCIS tumor slice motility assay was performed using an Olympus IX83 inverted microscope
1166 controlled by CellSens software (Olympus) and equipped with a iXon Ultra Andor (EMCCD) 16 bit
1167 camera using a UplanSApo 10X/0.4NA dry objective.
1168

1169 **Electron Microscopy**

1170 Electron microscopic examination was performed as previously described[6, 7]. A description of each
1171 process is described below.
1172 Embedding: the tissue and 3D spheroids were fixed with of 4% paraformaldehyde
1173 and 2.5% glutaraldehyde (EMS, USA) mixture in 0.2 M sodium cacodylate pH 7.2 for 2 hours at

1174 RT, followed by 6 washes in 0.2 sodium cacodylate pH 7.2 at RT. Then cells were incubated in 1:1
1175 mixture of 2% osmium tetraoxide and 3% potassium ferrocyanide for 1 hour at RT followed by 6
1176 times rinsing in 0.2 M cacodylate buffer. Then the samples were sequentially treated with 0.3%
1177 thiocarbohydrazide in 0.2 M cacodylate buffer for 10 min and 1% OsO4 in 0.2 M cacodylate buffer
1178 (pH 6,9) for 30 min. Then, samples were rinsed with 0.1 M sodium cacodylate (pH 6.9) buffer until
1179 all traces of the yellow osmium fixative have been removed, washed in de-ionized water, treated
1180 with 1% uranyl acetate in water for 1 h and washed in water again (Mironov et al., 2004;
1181 Beznoussenko et al., 2015). The samples were subsequently subjected to de-hydration in ethanol
1182 and then in acetone and embedded in Epoxy resin at RT and polymerized for at least 72 h in a 60 °C
1183 oven. Embedded samples were then sectioned with diamond knife (Diatome, Switzerland) using
1184 Leica ultramicrotome (Leica EM UC7; Leica Microsystems, Vienna). Sections were analyzed with
1185 a Tecnai 20 High Voltage EM (FEI, Thermo Fisher Scientific, Eindhoven, The Netherlands)
1186 operating at 200 kV[7].
1187

1188 **Measurement of the cellular velocities and trajectories on monolayers**

1189 Coarse-grained maps of the instantaneous cellular velocities were obtained by analysing time-lapse
1190 phase-contrast movies with a custom PIV software written in MATLAB[2]. The time interval between
1191 consecutive frames was 5 min or 10 min. The interrogation window was 32X32 pixels (pixel size
1192 1.29 µm or 1.6 µm), with an overlap of 50% between adjacent windows. The number of cell
1193 comprised within one field-of-view (FOV) was typically 2500. For a given monolayer, time-lapse
1194 images from different (typically from 5 to 10) FOVs were simultaneously collected.

1195 The instantaneous root mean square velocity $v_{RMS}(t)$ of a cell monolayer was computed as
1196 $v_{RMS}(t) = \sqrt{\langle |\boldsymbol{v}(t)|^2 \rangle_{\boldsymbol{x},j}}$, where is the instantaneous velocity vector $\boldsymbol{v}(t)$ and $\langle \cdot \rangle_{\boldsymbol{x},j}$ indicates an
1197 average over all grid points $\boldsymbol{x}$ (corresponding to the centers of the PIV interrogation windows) and
1198 FOVs j, respectively.

The instantaneous order parameter $\psi(t)$ of a cell monolayer was computed as $\psi(t) = \langle \frac{|\langle \boldsymbol{v}(t) \rangle_{\boldsymbol{x}}|^2}{\langle |\boldsymbol{v}(t)|^2 \rangle_{\boldsymbol{x}}} \rangle_j$. This definition is such that $0 \leq \psi(t) \leq 1$. In particular, $\psi(t) = 1$ only if, within each FOV, the velocity field is perfectly uniform, *i.e.* all the cells in the monolayer move with the same speed and in the same direction. On the contrary $\psi(t) \cong 0$ is expected for a randomly oriented velocity field.

The vectorial velocity correlation functions were calculated as $C_{VV}(r) = \langle \frac{|\langle \boldsymbol{v}(\boldsymbol{x}+\boldsymbol{r},t) \cdot \boldsymbol{v}(\boldsymbol{x},t) \rangle_{\boldsymbol{x},t}|^2}{\langle |\boldsymbol{v}|^2 \rangle_{\boldsymbol{x},t}} \rangle_j$. Unless otherwise stated in the main text, the temporal average $\langle \cdot \rangle_t$ was always performed over the time window comprised between 4 and 12 hours from the beginning of the image acquisition.

The velocity correlation function L_{corr} is obtained by fitting $C_{VV}(r)$ with a stretched exponential function of the form $f(r) = (1-\alpha)e^{-(r/L_{corr})^{\gamma}} + \alpha$. Here γ is a stretching exponent and α is an offset which is non-zero in presence of a collective migration of the monolayer.

Cellular trajectories $\boldsymbol{r}_m(t)$ were calculated by numerical integration of the instantaneous velocity field as obtained from the PIV analysis (see ref. [8] and reference therein). For each FOV a number of trajectories roughly corresponding to the number of cells was computed.

Mean squared displacements (MSDs) of the cells were calculated as $MSD(\Delta t) = \langle |\boldsymbol{r}_m(t+\Delta t) - \boldsymbol{r}_m(t)|^2 \rangle$, where the average was performed over all the trajectories and, unless otherwise stated in the main text, in the time window comprised between 4 and 12 hours after the beginning of the experiment. In order to estimate the persistence length L_{pers} of the cellular motion the MSD curves were fitted with a function of the form $g(\Delta t) = (u_0 \Delta t)^2 \left[1 + \left(u_0 \Delta t / L_{pers}\right)\right]^{-1}$. This expression describes a transition between a short-time ballistic-like scaling and a long-time diffusive scaling. The transition between the two regimes takes place for $\Delta t \approx 1/u_0 L_{pers}$, i.e. after the cell has travelled with an approximately constant velocity over a distance $\approx L_{pers}$.

Measurement of the cellular velocities of acini

Sequences of confocal Z stacks of 3D acini were analysed with an adapted PIV scheme in order to extract a representative value for the migration velocity, to assess the collective nature of the cellular motion and to detect the presence of a coherent rotational motion. Details about the imaging are given in the paragraph "Image acquisition".

The geometrical centre $\boldsymbol{x}_c$ of each acinus was determined as the centroid of the corresponding 3D fluorescent intensity distribution (Z stack) $I(\boldsymbol{x}|t)$, $\boldsymbol{x}_c = \frac{\sum I(\boldsymbol{x}|t)\boldsymbol{x}}{\sum I(\boldsymbol{x},t)}$, where the sum is performed over all voxels and time points. For each time point, the 3D fluorescent intensity distribution was radially projected onto the unit sphere centred in $\boldsymbol{x}_c$ leading to a sequence of 2D intensity maps $i(\theta,\varphi|t)$, where θ and φ are the polar and the azimuthal angle spanning the sphere, respectively. In practice, $i(\theta,\varphi|t)$ was obtained from a representation of $I(\boldsymbol{x}|t)$ in spherical coordinates, after summation over the radial coordinate. For each time point, i is represented by a 512x128 matrix, each element covering the Cartesian product of angular intervals of constant amplitudes $\Delta\,\theta = \pi/512$ and $\Delta\,\varphi = 2\pi/128$, respectively.

We performed on i a 2D PIV analysis as described in the previous paragraph, by treating (θ,φ) as Cartesian coordinates. The obtained coarse-grained velocity fields $[u_\theta(\theta,\varphi|t), u_\varphi(\theta,\varphi|t)]$ (in units of rad/hr) were then used to reconstruct the tangential velocity field $\boldsymbol{v}(\theta,\varphi) = R_0\left(u_\theta(\theta,\varphi|t)\boldsymbol{n}_\theta + u_\varphi(\theta,\varphi|t)\sin\theta\,\boldsymbol{n}_\varphi\right)$ of the acinus. Here, $\boldsymbol{n}_\theta$ and $\boldsymbol{n}_\varphi$ are the polar and the azimuthal unit vector, respectively and $R_0 = \sqrt{\frac{\sum I(\boldsymbol{x}|t)(\boldsymbol{x}-\boldsymbol{x}_c)^2}{\sum I(\boldsymbol{x},t)}}$ is the radius of gyration of the acinus.

The root mean squared velocity was calculated as $v_{RMS}(t) = \sqrt{\langle|\boldsymbol{v}|^2\rangle}$, where the angular brackets indicate an average performed over the whole sphere. The presence of a pattern of global rotation was monitored by measuring the total angular momentum $\boldsymbol{l} = \langle\boldsymbol{r}\times\boldsymbol{v}\rangle$, where $\boldsymbol{r}$ is a unit vector spanning the whole sphere. The direction of $\boldsymbol{l}$ identifies the orientation of the axis of instantaneous rotation. The collective nature of the cellular motility is captured by the non-dimensional rotational

order parameter $\psi = \frac{\pi}{2}\frac{|\boldsymbol{l}|^2}{v_{RMS}^2}$. The normalization of the order parameter is such that, for a rigidly rotating sphere, $\psi = 1$, while, in the absence of coordinated motion one expects $\psi \cong 0$.

Kinematic and dynamical analysis of spheroids

Overall motility and internal dynamics of the spheroids were measured by analysing sequences of confocal Z stacks, according to the following procedure, implemented in a custom MATLAB® code. More details about the imaging can be found in the paragraph "Image acquisition".

We indicate with $R(\boldsymbol{\Theta}, \boldsymbol{U})$ the roto-translational operator given by the composition of a 3D rotation by an angle $|\boldsymbol{\Theta}|$ around the axis identified by the direction of the 3D vector $\boldsymbol{\Theta}$ and a translation of vector $\boldsymbol{U}$. $R(\boldsymbol{\Theta}, \boldsymbol{U})$ is a linear operator and its numerical implementation as a transformation between 3D matrices (Z stacks) was realized *via* the MATLAB functions *imwrap* and *affine3d*.

Let us consider two 3D stacks $I(\boldsymbol{x}, t)$ and $I(\boldsymbol{x}, t + \Delta t_0)$, where Δt_0 is delay between consecutive stacks. We define $\boldsymbol{\Omega}(t)$ and $\boldsymbol{U}(t)$ as the 3D vectors that minimize the distance d (namely, the variance of the difference) between $I(\boldsymbol{x}, t + \Delta t_0)$ and $R(\boldsymbol{\omega}\Delta t_0, \boldsymbol{u})I(\boldsymbol{x}, t)$, $d(\boldsymbol{\omega}, \boldsymbol{u}|t) = \|I(\boldsymbol{x}, t + \Delta t_0) - R(\boldsymbol{\omega}\Delta t_0, \boldsymbol{u})I(\boldsymbol{x}, t)\|^2$. Numerically, the minimization is performed by exploiting the MATLAB function *imregtform*. In substance, $R\big(\boldsymbol{\Omega}(t)\Delta t_0, \boldsymbol{U}(t)\big)$ is the rigid transformation that reproduces at best the changes occurred in $I(\boldsymbol{x}, t)$ during the time interval Δt_0. According to the definitions above, $\boldsymbol{\Omega}(t)$ provides the best estimate for the instantaneous vectorial angular velocity of the spheroid, the direction of $\boldsymbol{n}(t) = \frac{\boldsymbol{\Omega}(t)}{|\boldsymbol{\Omega}(t)|}$ identifying the axis of instantaneous rotation. The temporal persistence of the rotational motion is captured by the orientational correlation function $C_{\boldsymbol{n}}(\Delta t) = \langle \boldsymbol{n}(t + \Delta t) \cdot \boldsymbol{n}(t) \rangle_t$, where $\Delta t = n\Delta t_0$. In order to estimate the rotational correlation time τ_P, $C_{\boldsymbol{n}}(\Delta t)$ was fitted with an exponential function of the form $f(\Delta t) = \exp(-\Delta t/\tau_P)$.

The non-rigid part of the changes occurring within a spheroid between time t and $t + \Delta t$, where $\Delta t = n\Delta t_0$, is captured by the parameter: $q(\Delta t, t) = 1 - \beta^{-1}\|I(\boldsymbol{x}, t + \Delta t) - T(\Delta t, t)I(\boldsymbol{x}, t)\|$, where

$T(\Delta t, t) = R(\boldsymbol{\Omega}(t + n\Delta t_0)\Delta t, \boldsymbol{U}(t + n\Delta t_0)) \circ R(\boldsymbol{\Omega}(t + (n-1)\Delta t_0)\Delta t, \boldsymbol{U}(t + (n-1)\Delta t_0)) \circ \ldots \circ R(\boldsymbol{\Omega}(\mathrm{t})\Delta t, \boldsymbol{U}(t))$ is the composition of elementary roto-translations and $\beta \equiv 2(\langle I^2 \rangle - \langle I \rangle^2)$. The definition of q is such that, neglecting noise and truncation errors, $q \cong 1$ if the spheroids is immobile or if it undergoes a perfectly rigid displacement and/or rotation, with no relative motion between different cells. On the contrary, one gets $q \cong 0$ when almost all the cells have performed positional rearrangements on a length scale comparable with their size, leading to a substantial change in the local structure[9]. We consider in particular the so-called overlap parameter Q, obtained as a temporal average of q: $Q(\Delta t) = \langle q(\Delta t, t) \rangle_t$. By fitting the decay of Q with an exponential function $Q(\Delta t) = Q_0 e^{-\Delta t/\tau}$ we can extract an estimate of the characteristic correlation time τ after which an almost complete change in the cellular configuration has occurred.

PIV analysis on ex vivo tumour slices

Maps of the instantaneous cellular velocities were obtained by analysing time-lapse movies by performing a PIV analysis using the MATLAB (Release R2017b The MathWorks, Inc., Natick, Massachusetts, United States) MPIV toolbox (http://www.oceanwave.jp/softwares/mpiv/)[10] with the correlation algorithm and an interrogation window of 24 pixels X 24 pixels (1 pixel = 1.4 um).

The analysis was performed on 3 independent experiments per condition on border sections of the tumour (for a total of 5 field of view per condition).

The instantaneous root mean square velocity $v_{RMS}(\mathrm{t})$ of a single Field of View was calculated as:

$$v_{RMS.}(\mathrm{t}) = \frac{1}{N}\sqrt{\sum_{n=1}^{N} |\boldsymbol{v}(\boldsymbol{x}_n, t)|^2}$$

1290

1291 where N is the number of grid points in the field of view and $\boldsymbol{v}(\boldsymbol{x}_n, t)$ is the instantaneous velocity at

1292 the *n*th grid point $\boldsymbol{x}_n$.

1293

1294 **Statistical analysis**

1295 Student's unpaired and paired t-test was used for determining the statistical significance. Significance

1296 was defined as $*p < 0.05$; $**p < 0.01$; $***p < 0.001$ and $****p < 0.0001$. Statistic calculations were

1297 performed with GraphPad Prism Software. Data are expressed as mean±SD, unless otherwise

1298 indicated.

1299

1300 **References (Methods)**

1301

1302 1. Komatsu, N. *et al.* Development of an optimized backbone of FRET biosensors for kinases
1303 and GTPases. *Mol Biol Cell* **22**, 4647-4656 (2011).
1304 2. Malinverno, C. *et al.* Endocytic reawakening of motility in jammed epithelia. *Nature*
1305 *materials* **16**, 587-596 (2017).
1306 3. Kardash, E., Bandemer, J. & Raz, E. Imaging protein activity in live embryos using
1307 fluorescence resonance energy transfer biosensors. *Nat Protoc* **6**, 1835-1846 (2011).
1308 4. Caldieri, G. *et al.* Reticulon 3-dependent ER-PM contact sites control EGFR nonclathrin
1309 endocytosis. *Science* **356**, 617-624 (2017).
1310 5. Sigismund, S. *et al.* Clathrin-mediated internalization is essential for sustained EGFR
1311 signaling but dispensable for degradation. *Dev Cell* **15**, 209-219 (2008).
1312 6. Beznoussenko, G.V., Ragnini-Wilson, A., Wilson, C. & Mironov, A.A. Three-dimensional
1313 and immune electron microscopic analysis of the secretory pathway in Saccharomyces
1314 cerevisiae. *Histochem Cell Biol* **146**, 515-527 (2016).
1315 7. Beznoussenko, G.V. & Mironov, A.A. Correlative video-light-electron microscopy of mobile
1316 organelles. *Methods Mol Biol* **1270**, 321-346 (2015).
1317 8. Park, J.A. *et al.* Unjamming and cell shape in the asthmatic airway epithelium. *Nature*
1318 *materials* **14**, 1040-1048 (2015).

9. Pastore, R., Pesce, G. & Caggioni, M. Differential Variance Analysis: a direct method to quantify and visualize dynamic heterogeneities. *Scientific reports* **7**, 43496 (2017).

10. Mori, N. & Chang, K.-A. Experimental Study of a Horizontal Jet in a Wavy Environment. *Journal of Engineering Mechanics* **129**, 1149-1155 (2003).